JINGLE, a JCMT legacy survey of dust and gas for galaxy evolution studies: II. SCUBA-2 850m data reduction and dust flux density catalogues

Journal Item

Monthly Notices
of the
ROYAL ASTRONOMICAL SOCIETY

MNRAS **486,** 4166–4185 (2019)
Advance Access publication 2019 April 17

doi:10.1093/mnras/stz1102

JINGLE, a JCMT legacy survey of dust and gas for galaxy evolution studies: II. SCUBA-2 850 μm data reduction and dust flux density catalogues

Matthew W. L. Smith [1★] Christopher J. R. Clark,[1,2] Ilse De Looze,[3,4] Isabella Lamperti,[3] Amélie Saintonge [3] Christine D. Wilson [5] Gioacchino Accurso,[3] Elias Brinks,[6] Martin Bureau,[7,8] Eun Jung Chung,[9] Phillip J. Cigan,[1] David L. Clements [10] Thavisha Dharmawardena,[11,12] Lapo Fanciullo,[11] Yang Gao,[13] Yu Gao,[14] Walter K. Gear,[1] Haley L. Gomez,[1] Joshua Greenslade,[10] Ho Seong Hwang [9,15] Francisca Kemper,[11,16] Jong Chul Lee,[9] Cheng Li,[17] Lihwai Lin,[11] Lijie Liu,[7] Dániel Cs. Molnár,[18,19] Angus Mok [20] Hsi-An Pan,[11] Mark Sargent,[18] Peter Scicluna [11] Connor M. A. Smith [1] Sheona Urquhart,[21] Thomas G. Williams [1] Ting Xiao,[13] Chentao Yang [14,22,23] and Ming Zhu[24]

Affiliations are listed at the end of the paper

Accepted 2019 April 13. Received 2019 April 12; in original form 2019 March 19

ABSTRACT

We present the SCUBA-2 850μm component of JINGLE, the new JCMT large survey for dust and gas in nearby galaxies, which with 193 galaxies is the largest targeted survey of nearby galaxies at 850 μm. We provide details of our SCUBA-2 data reduction pipeline, optimized for slightly extended sources, and including a calibration model adjusted to match conventions used in other far-infrared (FIR) data. We measure total integrated fluxes for the entire JINGLE sample in 10 infrared/submillimetre bands, including all WISE, *Herschel*-PACS, *Herschel*-SPIRE, and SCUBA-2 850 μm maps, statistically accounting for the contamination by CO(J = 3–2) in the 850 μm band. Of our initial sample of 193 galaxies, 191 are detected at 250 μm with a $\geq 5\sigma$ significance. In the SCUBA-2 850 μm band we detect 126 galaxies with $\geq 3\sigma$ significance. The distribution of the JINGLE galaxies in FIR/sub-millimetre colour–colour plots reveals that the sample is not well fit by single modified-blackbody models that assume a single dust-emissivity index (β). Instead, our new 850 μm data suggest either that a large fraction of our objects require $\beta < 1.5$, or that a model allowing for an excess of sub-mm emission (e.g. a broken dust emissivity law, or a very cold dust component $\lesssim$10 K) is required. We provide relations to convert FIR colours to dust temperature and β for JINGLE-like galaxies. For JINGLE the FIR colours correlate more strongly with star-formation rate surface-density rather than the stellar surface-density, suggesting heating of dust is greater due to younger rather than older stellar-populations, consistent with the low proportion of early-type galaxies in the sample.

Key words: galaxies: ISM – galaxies: photometry – galaxies: spiral – submillimetre: ISM.

1 INTRODUCTION

Studies of the interstellar medium (ISM) in large, varied galaxy samples are crucial to our understanding of star formation and galaxy evolution. Surveys of both atomic gas (via the H I 21 cm line) and molecular gas (often traced by emission lines of the CO molecule) have revealed that there are key scaling relations in the local Universe between global galaxy properties and the contents of the ISM (e.g. Roberts & Haynes 1994; Young et al. 1995; Catinella et al. 2010; Saintonge et al. 2011; Bothwell et al.

★ E-mail: matthew.Smith@astro.cf.ac.uk

2013; Boselli et al. 2014b). For example the Schmidt–Kennicutt law (Schmidt 1959; Kennicutt 1989) relates the surface density of star-formation to the surface density of gas in the galaxy. Large studies using H I, dust continuum emission in the far-infrared (FIR), CO, and other molecular line tracers have revealed that these scaling laws can depend on factors such as morphological type, mass, and environment (e.g. Cortese et al. 2011; Lisenfeld et al. 2011; Young et al. 2011; Cortese et al. 2012; Smith et al. 2012a; Rémy-Ruyer et al. 2014; Clark et al. 2015; De Vis et al. 2017)

Studies of dust in the ISM are important as over the lifetime of the Universe half of all light emitted from stars has been absorbed by dust and then re-emitted in the FIR (Lagache, Puget & Dole 2005). Stars are formed in dense clouds of gas and dust, and so FIR observations can be vital for measuring an accurate star-formation rate (SFR) in galaxies due to absorption of the UV and optical light (Kennicutt 1998; Calzetti 2001). Dust is important for molecules in the ISM as it catalyses reactions as atoms bind to the surface of dust grains (e.g. Gould & Salpeter 1963; Hagen, Allamandola & Greenberg 1979; van Dishoeck 2004). Given the difficulty with directly measuring molecular gas with CO or other tracers, and this especially at high redshifts, dust is also seen as a promising probe of the entire cold ISM (e.g. Guelin et al. 1993, 1995; Israel 1997; Scoville et al. 2014).

While there have been surveys with observations of H I, CO, and dust continuum, they are the exceptions. One example is the SINGS sample (Kennicutt et al. 2003) which targeted ∼70 galaxies with distances <30 Mpc, obtaining dust continuum data with *Herschel* (KINGFISH; Kennicutt et al. 2011), and exquisite gas measurements in H I (THINGS; Walter et al. 2008) and CO (HERACLES; Leroy et al. 2009). Another example is the *Herschel* Reference Survey (HRS; Boselli et al. 2010a) which targeted 322 *K*-band selected galaxies in a volume-limited sample, and has collected data on all three components of the cold ISM (Ciesla et al. 2012; Cortese et al. 2014; Boselli, Cortese & Boquien 2014a). To make sure to sample a full range of galaxy properties, large statistical samples beyond the very local Universe focusing on these different components of the cold ISM are required. Using the James Clark Maxwell Telescope (JCMT), the JCMT dust and gas In Nearby Galaxies Legacy Exploration (JINGLE; Saintonge et al. 2018, hereafter Paper I), aims to address this. JINGLE has observed dust continuum at 850μm for 193 SDSS-selected galaxies ($M_* > 10^9$ M$_\odot$), and CO(J = 2–1) line emission for a subset of ∼35 per cent of them. The sample was selected in fields with coverage from *Herschel*–ATLAS (hereafter *H*-ATLAS; Eales et al. 2010), which observes between 100 and 500 μm, the Arecibo ALFALFA H I survey (Giovanelli et al. 2005), and the MaNGA and SAMI optical integral field spectroscopic surveys (Bryant et al. 2015; Bundy et al. 2015), providing additionally the all- important information about dust, atomic gas, ionized gas, and resolved stellar properties.

The SCUBA-2 data (the subject of this paper) of 193 galaxies is the largest targeted survey of nearby galaxies at 850 μm. Adding a data point far down the Rayleigh–Jeans tail provides an improvement on obtaining dust measurements, over just using *Herschel* data between 70 and 500 μm. For example, there can be a degeneracy in fitted parameters between the dust emissivity index (β, see Section 6.3) and dust temperature measured (Smith et al. 2012b). By adding a data point at 850 μm further down the Rayleigh–Jeans tail of blackbody emission the degeneracy can be reduced by approximately a factor of two. An additional benefit is that the *Herschel* SPIRE calibration is dominated by correlated uncertainties (4 per cent correlated versus 1.5 per cent uncorrelated) between bands due to uncertainties in planet models (Bendo et al. 2013), which can have a significant effect on SED fitting results. With an independent longer wavelength point at 850 μm (as SCUBA-2 uses different calibrators) we can obtain a more accurate measurement of β, which is important as it can be an indication of grain size, composition, or surface mantles. Differences in the assumed numerical value of β can have a significant effect on the dust-mass absorption coefficient (κ_d) and consequently on the dust masses that are inferred from FIR observations (e.g. Bianchi 2013; Clark et al. 2016).

In this paper, we present our observing strategy (Section 2.2) and our customized data reduction pipeline, which is optimized for the specific requirements of the JINGLE survey (see Section 3). In Section 4, we describe our flux extraction methods for both point and extended sources, and describe our simulations to account for any flux attenuation from the pipeline high-pass filter. Section 5 describes our approach to remove CO(J = 3–2) contamination of our 850 μm fluxes. Finally, in Section 6 we investigate FIR/submm colour ratios, and how they relate to model fits of temperature, dust emissivity, and other physical properties of the galaxy.

2 SAMPLE AND OBSERVATIONS

2.1 JINGLE sample overview

The sources in the JINGLE survey are selected based on detections from the *H*-ATLAS survey (Eales et al. 2010) which observed ∼600 deg^2 with *Herschel* (Pilbratt et al. 2010). *H*-ATLAS observed in parallel mode using PACS at 100 and 160 μm, and SPIRE at 250, 350, and 500 μm simultaneously. As JCMT is in the Northern hemisphere, JINGLE selected objects in the equatorial GAMA fields (161 deg^2) and the North Galactic Pole (NGP) field (180.1 deg^2). For our photometry (Section 4) we use the PACS maps provided in *H*-ATLAS DR1 (GAMA fields, Valiante et al. 2016) and DR2 (NGP; Smith et al. 2017). For SPIRE we use the same timelines used to generate the maps in the DR1 and DR2 releases, except we apply the relative gain corrections and calibration corrections to optimize the maps for extended sources (these maps are also made available in the JINGLE data release).

2.2 SCUBA-2 observations

In this section, we outline the strategy used by the JINGLE survey to obtain good-quality maps at 850 μm with SCUBA-2 (we also simultaneously obtain 450 μm but as the sensitivity is lower than SPIRE 500 μm we only concentrate on 850 μm in this work). The redshift selection of the JINGLE survey ($0.01 < z < 0.05$) puts our targets at a distance of ∼41–212 Mpc with a mean D_{25} (the *B*-band isophotal diameter at a surface brightness of 25 mag arcsec^{-2}) of 1.28 arcmin, with the largest size of 4.6 arcmin. However, from the SPIRE 250 μm maps the largest aperture required to accurately measure the flux of our objects has a diameter of 2.2 arcmin. For all JINGLE targets we therefore observe using the 'Constant Velocity (CV) Daisy' mapping mode which is the smallest observing mode available with SCUBA-2, and provides an even coverage in the central 3 arcmin of the observation. The 'CV Daisy' is a circular scanning pattern designed so that the target is always within the field-of-view of the array throughout the integration while moving at a constant 155 arcsec s^{-1}. The observation provides useable coverage out to ∼6.0 arcmin in radius, but beyond 1.5 arcmin the map sensitivity decreases rapidly. A typical weight map ($1/\sigma^2$) for a JINGLE Daisy observation is shown in Fig. 1.

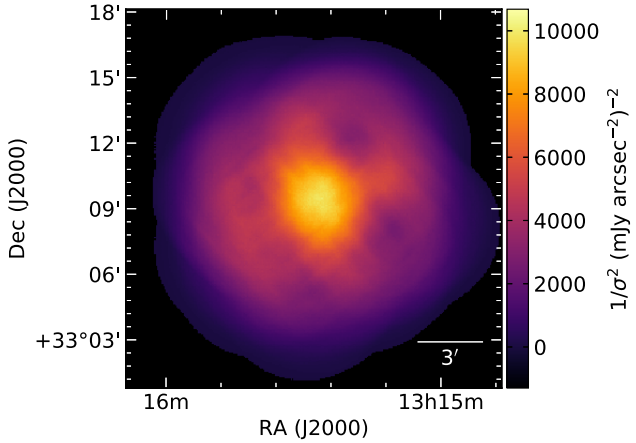

Figure 1. An example weight image for a typical observation, which illustrates how the sensitivity of our observation decreases with radius. The weight image is calculated from the inverse square of the noise.

The sensitivity estimates for each JINGLE target were derived by fitting a modified-blackbody model to the *Herschel* data (fluxes were taken from an initial *H*-ATLAS catalogue). As literature values of the dust-emissivity index (β) tend to lie in the region 1.5–2.0 (Planck Collaboration XVII 2011; Smith et al. 2012b; Cortese et al. 2014; Planck Collaboration XIV 2014), we use a constant value of $\beta = 2$, which should be a conservative estimate of the 850 μm flux. To account for JINGLE galaxies being extended we use the radius of the galaxy to divide the total flux evenly between 1 and 8 independent elements. The SCUBA-2 exposure time calculator was then used to calculate the total integration time required to achieve a signal-to-noise ratio of 5. The estimates were made assuming matched-filtering which as we discuss in Section 3 is not appropriate for our data, this is slightly compensated by our decision to use pixel sizes larger than the 1 arcsec default (when the survey was proposed) in the integration time calculator. The weather band (dependent on the amount of water vapour in the atmosphere) was chosen so the total integration time is always under 2 h. Overall our observations were generally taken in slightly better conditions than assumed when using the exposure time calculator.

3 DATA REDUCTION

The JINGLE survey was designed specifically so as to minimize problems with emission on large scales, which has been a problem with ground-based imaging due to atmospheric and instrumental variations often requiring spatial filtering to be applied. To try avoid this issue the minimum redshift of $z > 0.01$ is used to select targets without large angular sizes. However, by having isolated objects which are resolved, but do not have extended structures (like galactic regions or very-nearby galaxies) means JINGLE is between the two extremes of point sources or preserving large-scale emission for which SCUBA-2 pipelines have been developed. We therefore, have worked to customize the data reduction pipeline for our specific case of marginally resolved objects. In this section, we describe our customized pipeline.

3.1 SCUBA-2 data processing

To reduce the raw SCUBA-2 data and create maps, we use the default SCUBA-2 map-maker MAKEMAP provided as part of the STARLINK software package (Currie et al. 2014).[1] We refer to Chapin et al. (2013) for full details of the MAKEMAP algorithm, but briefly, after an initial 'cleaning' stage, which removes bad bolometers and artefacts such as glitches, MAKEMAP begins an iterative procedure to split the bolometer signals into various components. In each iteration a 'common-mode' signal predominately from sky noise is identified and subtracted, an extinction correction is applied, and then the bolometer signals are high-pass filtered. From these timelines (time-ordered detector readouts) a map is made to identify astronomical emission (AST model) which is subtracted from the next iteration. This iterative procedure continues until the map converges (see below), or reaches the maximum number of iterations. This technique is highly customizable, allowing settings at every step to be adjusted to optimize the data for your science target. Below we describe how we optimized the JINGLE data for our case of slightly extended sources.

The standard MAKEMAP implementation processes each observation individually and then combines the individual maps at the end. If the memory requirements are too big for a machine, the observation is split into 'chunks', each processed separately (note for all JINGLE processing a machine with enough memory is used so no 'chunking' is required). While this is computationally efficient it does not make best use of the data, instead the astronomical model in each iteration should be estimated from all the observations due to improved sensitivity and better resilience to atmospheric/instrumental variations. The SKYLOOP script provided in STARLINK solves this problem, and is designed to help recover more signal, by using all the data at the end of every iteration. Our script is modified from the standard SKYLOOP as we found that for all but the first observation passed to MAKEMAP, the proportion of data flagged became excessively high. We modified the script to output a map for each observation after every iteration and then mosaic the data, instead of feeding all the data to MAKEMAP in one go. After discussions with the observatory, SKYLOOP in the STARLINK 2017A package has been updated so this problem no longer exists.

The second difference is our method to apply source masking to the data. In SCUBA-2 terminology 'Masking' is where regions are selected where the AST model is allowed to vary, in any other area of the observation the AST model is set to zero. This improves the reduction as it helps to reduce any degeneracies between AST and other noise models. Such masks can be static (i.e. fixed for all iterations) or dynamic where the mask is generated based on some threshold in the map at each configuration. For JINGLE due to the high-sensitivity of *Herschel* SPIRE observations we have very good prior knowledge of where we expect to find emission at 450 and 850 μm, and can be confident we can select regions without missing any sub-millimetre emission. This masking is very effective for our targets as our galaxies are isolated nearby sources and we therefore use the surrounding areas as background. Unlike other surveys which apply a two-pass approach, where they perform an initial run to create a fixed mask by reducing the data either without a mask or with an adaptive mask, through the use of our SPIRE data we can use our fixed mask. We generate a 2D-image as an input mask which has the advantage over the standard *ast.zero_circle* parameter in MAKEMAP that we can use elliptical shapes and include multiple sources. Our source ellipse is based on the size of the aperture used for our FIR photometry which we describe in detail in Section 4.

The behaviour of MAKEMAP is controlled using a configuration file which specifies all the settings to optimize the map-maker for

[1] All maps were created using STARLINK package version 2017A.

the science required. The JINGLE DR1 configuration file is made up of the following commands:

(i) *numiter = −300 and maptol = 0.001* – Mairs et al. (2015) found for The JCMT Gould Belt Survey (Ward-Thompson et al. 2007) that a stricter convergence tolerance helped recover more low-surface brightness structure in their maps. Whether a map has converged is set by the *maptol* parameter which is the threshold value for the mean change of the map between iterations normalized by the root-mean-square of the pixel variances (i.e. when the map stops changing, note that this is calculated from regions not masked). The default of this parameter value is set to 0.05 and so the value of 0.001 is a much more stringent criterion. Like Mairs et al. (2015) to compensate for this stricter limit we increase the number of allowed iterations from a typical value of ∼40–300 (the minus sign in the parameter allows the map to finish if converged, otherwise all iterations would be performed). We found that with our masking we normally converge reasonably quickly (∼20 iterations).

(ii) *com.perarray = 1* – This parameter controls whether the 'common-mode' component (i.e. atmosphere or instrument variations) is required to be the same across the whole array or whether each sub-array is treated independently. We choose to set this so each sub-array is treated independently; this can remove emission scales above the size of a sub-array (∼3 arcmin), but as we filter at smaller scales we can safely treat each sub-array independently.

(iii) *flt.filt_edge_largescale = 150* – This parameter has possibly the largest effect when creating SCUBA-2 maps as it controls the scale (in arcsec) of the high-pass filtering applied to the data. If set too high, spurious signals from the atmosphere or drifts in the array could dominate the astronomical signal; however, if set too low the filtering could remove a significant fraction of the source's emission. Fig. 2 shows one extreme example of the effect of the filter scale when we were testing our data reduction. When the filter scale was set to 100 arcsec, JINGLE 119 was not detected in our pipeline. After experimenting with a test sample of objects we settled on a filter scale of 150 arcsec as the best compromise between sensitivity and recovering the flux. In Section 4.3, we describe our simulations to quantity the exact effect of the filtering on each source.

(iv) *ast.zero_mask = 1 and ast.zero_snr = 0* – These parameters set MAKEMAP to use a static mask (as described above) using a file specified by the REF parameter, and to not apply a threshold to the pixels within this mask to be included in the AST model. Specifying a file via the REF parameter sets the world coordinate system (WCS) for the output image to match the static mask.

(v) *ast.zero_freeze = 0, com.zero_freeze = 0, and flt.zero_freeze = 0* – These are the default values which state that we do not freeze the AST, common-mode signal (COM), or low-frequency Fourier component (FLT), models after any iteration. These parameters are included as a previous version of skyloop required these parameters to be explicitly set.

We also investigated whether we should set the FLT mask using the same mask defined for the AST model (using the *flt.zero_mask* = 1). In the regions set by the FLT mask the detector timelines are replaced by a linear interpolation before the high-pass filter is applied, with the aim of avoiding ringing around the source. By default this is only applied for the first two iterations and so the signal can be identified in the AST model. We found that this had a large effect on our maps with our extracted flux densities being on average a factor of two higher than our predicted 850 μm fluxes, derived extrapolating modified blackbody fits to *Herschel* ≤500 μm flux densities. However, our standard reduction agreed well with our predictions (this agrees with our simulations injecting sources into the map in Section 4.3). For some JINGLE targets setting the FLT mask resulted in an 850 μm flux density higher than the SPIRE 500 μm flux, which for a standard local galaxy (with no radio contamination) would be un-physical. As such we do not set the FLT mask for our reduction, with the exception of JINGLE 70 and 132 which in our standard reduction resulted in very significant negative fluxes (-4.7σ and -7.5σ). Setting the FLT mask in these two cases removed the negative artefact and gave fluxes in line with our predictions.

3.2 Calibration

The standard procedure at the JCMT is to take a few calibration observations spread over the evening which can be used to see if there are any changes or particular problems over the night. JINGLE calibration observations are based on either Mars, Uranus, CRL618, CRL2688, or Arp220 depending on source visibility. There are good reasons to assume the calibration does vary throughout the night, as the dish cools at the beginning of the night. As the pipeline is very flexible the standard advice is to apply the same procedure to your calibrators as adopted for the target object. For example, the default is to use a 30 arcsec radius aperture for your source and calibrator. However, while this advice is sensible for point sources, it becomes problematic for extended sources where different fractions of the source will be present in apertures, and filtering will have a different effect based on the amount being masked. We instead decide to take an alternative approach, where we optimize the reduction of the calibrators to give the most accurate calibration of our maps (i.e. the calibration that results in the true flux densities of our targets if no attenuation of large angular scales occurs), and then simulate the effect of filtering on our individual targets.

To investigate the calibration we look at calibration observations from the beginning of the project to 2016 December, when we had observed just over half the SCUBA-2 sample. When making maps of our calibrators, the aim was to use as similar as possible configuration file as used for our targets; however, some adjustments were required. We discovered when creating maps of our calibrators that, in particular for Mars, the centre of the source was clipped due to the cleaning process. To mitigate this effect we set the *ast.mapspike* parameter to 10, which controls the signal-to-noise of detector samples to remove from a map-pixel, and the *dcthresh* parameter which controls the signal-to-noise ratio of DC step detection to 10 000. As the calibration observations are centred on the calibrators, and the sources are all point-like in SCUBA-2 images we set the *ast.zero_circle* and *flt.zero_circle* to 2 arcmin, which sets the static mask (see Section 3.1) of the AST and FLT models to a circle in the centre of the image. As with our target map-making in Section 3.1, one of the most important parameters is the filter-scale parameter (*flt.filt_edge_largescale*). Ideally, the filter scale would be set to a very high value so the flux of our calibrator is not attenuated; however, as the calibration observations are short for our dimmer calibrators this would lead to the measurement being dominated by large-scale noise on the map. To test the optimum filter-scale so that our calibrators are not attenuated we take two independent observations of Mars (our brightest calibrator) and create a map for filter-scales from 100 to 200 arcsec in 10 arcsec intervals and then from 200 to 400 arcsec in 20 arcsec intervals. Fig. 3 shows the fraction of flux measured depending on the filter-scale. From these results we chose to filter our calibrator observations on a scale of 220 arcsec as this is safely on the plateau, but small enough to provide a flat background in the map, and we set *com.perarray* to 0.

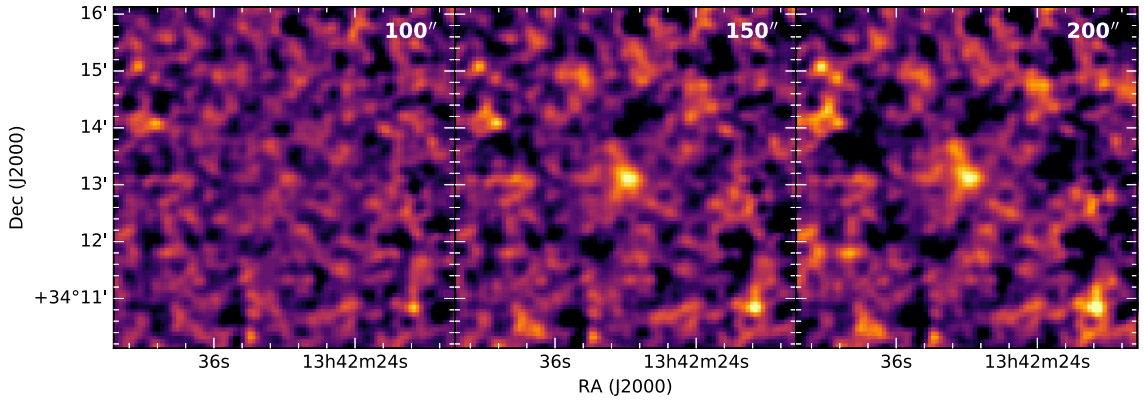

Figure 2. An example of how different filter scales (as set by the *flt.filt_edge_largescale* parameter) affect the resulting SCUBA-2 850 μm map for JINGLE 119. When a 100 arcsec filter (left) is applied our target is filtered out of the map, but increasing the filtering to 200 arcsec (right) leads to increased noise.

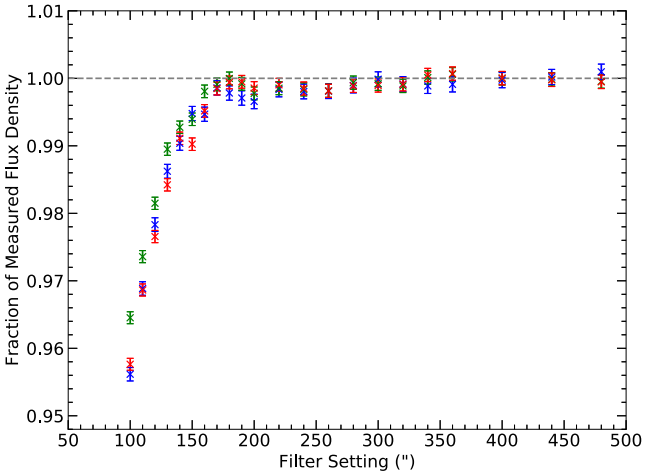

Figure 3. The fraction of flux measured compared to the average value measured in maps where the filter-scale has been set to >350 arcsec. The blue points correspond to observation id 20151226_00069 with the com.perarray set to 0, the green and red points both correspond to observation id 20151227_00067 with the com.perarray set to 0 (green) and 1 (red).

To calculate the flux conversion factor (FCF) from our calibrator maps we run the standard PICARD recipe SCUBA2_CHECK_CAL which uses the default settings which matches the method used by Dempsey et al. (2013) who calculated the standard FCF values. As our sources are extended we calibrate our maps in units of mJy arcsec^{-2} rather than mJy beam^{-1}. Fig. 4 shows the ratio of FCFs to the standard value obtained at 850 μm for our calibrators. The median ratio for our calibrators is 1.002 suggesting our observations are consistent with the standard, although we find the scatter for Arp 220 is significantly larger than the other sources, probably due to it being one of the fainter calibrators. The scatter in FCF values result in a calibration uncertainty of 5.7 per cent, similar to the value of 5 per cent found in Dempsey et al. (2013).

The FCF values in Fig. 4 are plotted against the time in the day the observation was taken. We see no obvious trend to suggest the FCF is higher at the beginning of the night. However, to check whether using a variable calibration leads to an improvement over assuming a fixed calibration we reduce all maps using both methods. For the variable case we calculate the FCF for each observation based on the linear interpolation between the calibration observation before and after the JINGLE observation (if observations are not available before and after we use the nearest calibration value). As SKYLOOP takes all the data simultaneously we multiply the raw data for each science observation by the ratio of our variable FCF to standard FCF and then apply the standard FCF to the resultant map from SKYLOOP. To see if there is any improvement in the map we see if there is any reduction in the uncertainty map (accounting for the difference in average FCF value). We did not see any maps with a significant improvement and so have decided to use our fixed values. We will re-visit this in subsequent works where we use the 450 μm data, where the calibration is more likely to vary.

The standard PICARD recipe to calculate the FCF uses a 30 arcsec radius aperture with a background annulus between radii of 45–60 arcsec. While these apertures were chosen as a good compromise between encircling enough of the emission and achieving a good signal-to-noise, it systematically overestimates the FCF as it does not account for the fraction of the beam outside the aperture. We decided to modify our FCF value to account for this aperture correction, so our images match the calibration scheme of our other FIR data sets. To find this correction we use the measurements that characterize the SCUBA-2 beam from Dempsey et al. (2013), who find it is well described by the sum of two Gaussians, the primary beam with a 13.0 arcsec full width at half-maximum (FWHM) and a secondary with a 48 arcsec FWHM. By integrating the beam profile from a radius (r) of zero to infinity and within radii of 0–30 arcsec and 45–60 arcsec, we calculate what fraction of the beam is outside the standard aperture and the amount included within the background region. We calculate that the FCF should be multiplied by a factor of 0.910 (this is in reasonable agreement with values measured by, Dempsey et al. 2013) and so we apply an FCF of 2.134 Jy pW^{-1} arcsec^{-2}.

3.3 WCS correction

For a few objects we found cases where there appeared to be an offset between where we expected to see emission at 850 μm from images at other wavelengths (e.g. *Herschel*). After investigating potential cases we found four cases where small offsets seen in our observations were also seen in either the pointing or flux calibration observation performed after the science observations. From these observations we derive offsets of 3.91, 4.17, and 5.22 arcsec for JINGLE 35 (J131958.31+281449.3), JINGLE 149 (J125610.97+280947.4), and JINGLE 186 (J132035.40340821.7), respectively. For JINGLE 117, observations on two separate days were found to have offsets of 6.84 and 4.43 arcsec, therefore these

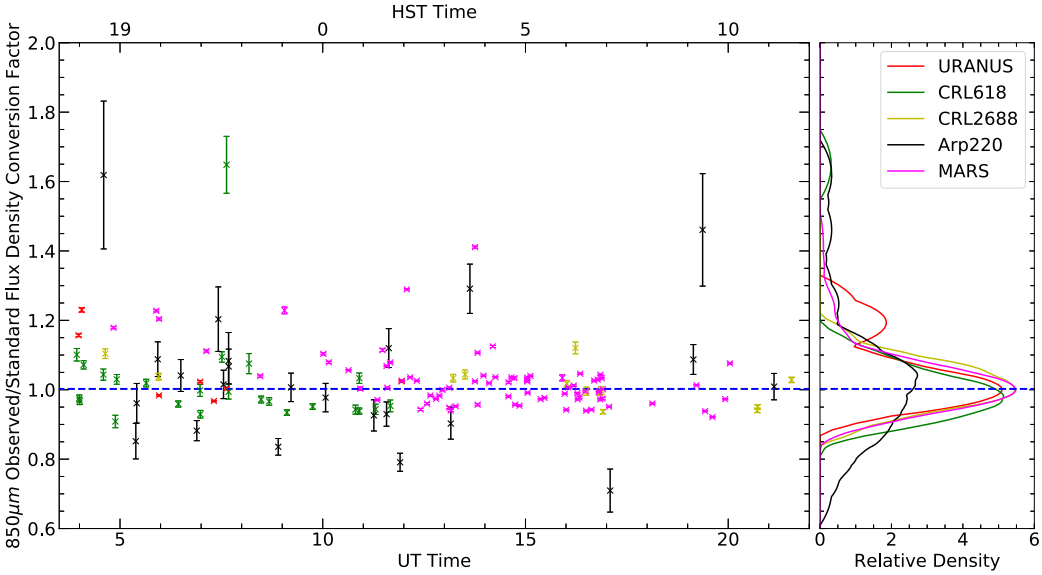

Figure 4. Flux conversion factors (FCFs) measured either before or after JINGLE observations at 850 μm up to 2016 December, calculated from observations of Mars (magenta), Uranus (red), CRL618 (green), CRL2688 (yellow), and Arp220 (black). The blue line shows the median value of all our observed FCF values which is in very good agreement with the standard FCF value (1.002×). From the kernel density estimation (KDE) graph (right) we see that most of the calibration sources agree well with each other, although Arp220 being a dimmer source has a larger scatter. The data points are ordered by the time they were observed; we see no obvious trends.

corrections are applied to the raw timeline data, before the map-making procedure.

3.4 Individual galaxy considerations

For the full JINGLE survey there are seven pairs of JINGLE targets and one triple system, where the JINGLE SCUBA-2 observations of each individual target overlap. As the full sensitivity region of Daisy maps is quite small and the only other map modes are significantly bigger and limited to circular observations, we decided to observe these targets fully. These objects are processed together to make full use of the overlapping data, as the greater redundancy is useful for identifying and removing atmospheric and instrumental noise.

For three galaxies (JINGLE 45, 119, 150) we found partially overlapping observations in the archive from M13AN02 (Ivison et al. 2016) and M18AP013 (a JINGLE extension program), targeting other sources. For these galaxies combining the serendipitous observations with the JINGLE data, leads to an ∼12, 5, and 26 per cent improvement in the instrumental noise for JINGLE 45, 119, 150, respectively.

We also inspected the SPIRE maps and our initial SCUBA-2 maps to see if there were other bright objects in the field that should be included in the input mask. The serendipitously detected bright high-redshift objects described in Paper I were also added to the mask and the maps re-run to ensure their flux was not suppressed.

To test our choice of filter correction we also ran a reduction of the maps where we varied the filter scales to a value of 175 arcsec for all galaxies and 200 arcsec for a selection of objects. For five galaxies we found a significant change in the flux measurement which were identified as cases in our 150 arcsec reduction where we find strong negative regions usually around a central source, often leading to a negative flux estimation. For JINGLE 45 we therefore use the map filtered at 175 arcsec and for JINGLE 19, 44, 154, and 185, we use maps filtered at 200 arcsec.

The 193 SCUBA-2 maps described here, as well as the WISE, PACS, and SPIRE cut-outs of our targets are available on the JINGLE data release page.[2] We also provide SCUBA-2 maps that have been Gaussian smoothed with either an FWHM of 12 and 24 arcsec, and a map generated by applying the PICARD matched-filtered algorithm which creates a map optimized for the detection of point sources. The code used to perform the data reduction is available on GitHub.[3]

4 FAR-INFRARED/SUB-MM FLUX EXTRACTION

4.1 Photometry

Here we describe our method of deriving flux densities in the FIR and sub-mm (22–850 μm). To extract flux densities from the *Herschel*, *WISE*, and SCUBA-2 maps we perform aperture photometry on the dust images separately from the procedures used at shorter wavelengths (i.e. UV, optical) presented in Paper I as our dust images (particularly in the SCUBA-2 bands) have reduced signal-to-noise, due to the difficulties in observing in the FIR/sub-mm. Instead we decide to have a consistent set of apertures optimized on the dust data, rather than the larger apertures that would be derived from optical wavelengths. These flux-densities are therefore ideal for the analysis of the dust properties of galaxies (i.e. FIR dust SED fitting).

The size and fluxes from our dust apertures are generated by an automated code, but a large degree of manual customization is allowed to remove problems that arise (for example other bright objects or map artefacts). To define our apertures we use the SPIRE 250 μm band, as at this wavelength we have the greatest sensitivity

[2] http://www.star.ucl.ac.uk/JINGLE/data.html
[3] https://github.com/mwls/SCUBA2-public

to dust structures. For the first step an automatic mask is created to remove the influence of any other bright nearby galaxy. We do this by performing a query on the RC3 catalogue (Corwin, Buta & de Vaucouleurs 1994) and masking all pixels within a radius of $2.0\,R_{25}$, which will safely mask the vast majority of dust contamination (Smith et al. 2016). If other bright contaminating objects are found on the image their positions and sizes can be manually added to the mask. An initial noise estimate of the image is then calculated using an iterative sigma-clipping technique. This rough noise is then used to find all contiguous pixels above a given signal-to-noise (set to a default of 3) within a region with $R < 0.5\,R_{25}$. The smallest ellipse which fits these pixels is then used to define the centre, the axes ratio, and the position angle (PA) of the ellipse. If no significant pixels exist, or the shape cannot be found, we default to the optical centre, the D_{25} axial ratio, and PA, from the RC3 catalogue. Using these parameters, and our rough noise estimates we then create a radial profile assuming a default background radius between 1.1 and $1.4\,R_{25}$. If the galaxy is above our detection criterion of a signal-to-noise of 3 then the object is preliminarily classed as a detection and the preliminary size of the aperture is determined by the radius at which our radial surface-brightness ratio crosses a signal-to-noise of 2, and multiplied by a default factor of 1.2 (this can be adjusted for special cases, i.e. to avoid contaminating objects) to ensure we enclose most of the emission.

To calculate the final aperture we need to make a better estimate of the noise in the image. To do this we use an estimate based on the method presented in Smith (2013) and Ciesla et al. (2012), where we consider the instrumental noise, confusion noise, and background error separately. The instrumental noise is found using the 'error' extension provided with the maps, which are typically calculated based on the standard deviation of samples contributing to that pixels. As a full map is available the exact instrumental noise for a particular aperture is calculated by adding the pixels in the noise map in quadrature. As the confusion noise is not independent between pixels (as pixels are smaller than the beam), the confusion noise is calculated based on the square-root of the number of beams within the aperture. The third contribution is from large-scale backgrounds, including cirrus contamination. The method employed to measure the large-scale background by Ciesla et al. (2012) was very conservative and led to an overestimate of the uncertainty (see Smith 2013). We therefore modify this approach and instead use NEBULISER,[4] also used by the *H*-ATLAS team (Valiante et al. 2016), which filters the map based on a threshold radius into small scale and large scale. We set this threshold to 90 arcsec in the SPIRE bands. We then use our large-scale map (or effectively cirrus map) and place a series of aperture across the image with the same size, shape, and background region as our preliminary aperture on the cirrus map, and obtain the standard deviation of these apertures. Using NEBULISER in this way prevents us counting the same noise components multiple times. Ideally, these apertures would be randomly placed, but as some images are limited in size (especially in the SCUBA-2 bands), and we are primarily interested in local conditions, we use a grid of apertures around the target source (again avoiding other nearby galaxies). We scale this estimate for the relative number of pixels in our final aperture, which should be accurate assuming that the size of our preliminary aperture is similar to our final result.

[4]http://casu.ast.cam.ac.uk/surveys-projects/software-release/background-filtering

As the point spread function (PSF) in FIR instruments can have significant extended features, we apply aperture corrections. These can be quite large factors, as even though the emission is low-surface brightness, the emission can be spread over a large area, and can contaminate background regions leading to an oversubtraction of the flux. As dust is expected to be distributed roughly in dust discs (Pohlen et al. 2010; Hunt et al. 2015; Smith et al. 2016), we fit an exponential plus constant model using the same PA and axis-ratio as the pixels within the aperture. In the fitting process each trial model is convolved with the radially averaged beam. By using our model within the aperture, we then predict the amount of emission outside the aperture, correcting our flux for the missing emission, and the effect of emission in the background region. For bands with lower resolution we use the model parameters found from the 250 μm image and convolve the model with the appropriate beam (see Table 1 for whether the model was fit in each band).

While for the vast majority of objects in our sample the automated apertures are valid, a small subset (15) of objects require us to lock the centre to the optical centre. For 16 galaxies we lowered the default aperture expansion-factor of 1.2, although the factor is never set to be less than 1.0. These changes were often made to avoid problems from nearby background sources or other contaminating features.

In bands other than the SPIRE 250 μm, we use a matched aperture to the 250 μm band, except we correct for the difference in beam size by modifying the size of the semimajor and semiminor axis. This is achieved by taking the 250 μm aperture size and subtracting in quadrature the 250 μm FWHM/2 and adding the current band's FWHM/2. Finally a useful diagnostic graphic is created showing the images with apertures, the resultant fluxes, peak signal-to-noise ratios, aperture corrections, the radial profile, and growth curves. An example of this image is shown for JINGLE 122 in both SPIRE (Fig. 5) and SCUBA-2 (Fig. 6) wavebands.

Confusion measurements for SCUBA-2 are difficult as surveys of galaxies at higher redshifts apply matched filtering to optimize the detection of point sources. This convolution changes the confusion noise measured on the map. To find the confusion noise we perform a simulation where we create a fake map that just contains confusion noise, and then apply the SCUBA-2 match filter. We vary the level of confusion until the amount of confusion noise in the raw map matches the 0.8 mJy beam^{-1} measured by the SCUBA-2 Cosmology Legacy Survey (Geach et al. 2017). As part of our test we also check how the confusion noise scales with aperture size, we found that for SCUBA-2 assuming the contribution of confusion varying as $\sigma_{\rm conf}\sqrt{N_{\rm beam}}$ did not represent the noise adequately, instead we use $\sigma_{\rm conf}\sqrt{N_{\rm beam}} - {\rm const}$ where $\sigma_{\rm conf}$ is 1.22 mJy beam^{-1} and const is −0.61. Table 1 lists the beam area, confusion noise, and NEBULISER filter scale assumed for the flux density measurement in each band.

Both JINGLE 57 and 60 at 850 μm were found to have significant contamination within the aperture from a point source presumably at a higher redshift. To remove the contamination we fit the point source using the same procedure outlined in Section 4.2, and then subtract the source from the image. We then run the aperture code as normal on the subtracted image. A more complicated case is JINGLE 29 where the more compact early-type object overlaps with a more flocculent late-type galaxy. To separate these objects we use the typical size of dust-discs based on the D_{25} from Smith et al. (2012a) to choose a region that likely encompasses the extent of emission from JINGLE 29, this also agreed with the region that would be chosen visually. Then all

Table 1. Individual band parameters.

Instrument	Band	FWHM (arcsec)	Beam area (arcsec^2)	Confusion noise (mJy beam^{-1})	NEBULISER median filter (arcsec)
SPIRE	250 μm	17.6	469.7	5.8	90
	350 μm	23.9	831.7	6.3	90
	500 μm	35.2	1793.5	6.8	90
PACS	100 μm	11.4	147.2[a]	0.27	60
	160 μm	13.7	212.7[a]	0.92	60
WISE	3.4 μm	6.1	42.2[a]	–	60
	4.6 μm	6.4	46.4[a]	–	60
	12 μm	6.5	47.9[a]	–	60
	22 μm	12.0	163.2[a]	–	60
SCUBA-2	850 μm	13.0	229.5	($m = 1.22$, $c = -0.61$)[b]	60

Notes. For the WISE wavelengths we assume the contribution of confusion noise is negligible and so set to zero in the code. Confusion noise estimates for SPIRE were taken from Nguyen et al. (2010), with the PACS FWHM, beam areas and confusion noise taken from Smith et al. (2017).
[a]These beam areas assume a Gaussian beam profile calculated from the FWHM. These instruments are not calibrated in Jy beam^{-1} (or similar), but the conversion is used just to scale the confusion noise (where appropriate).
[b]See Section 4.1 for details on the SCUBA-2 confusion noise.

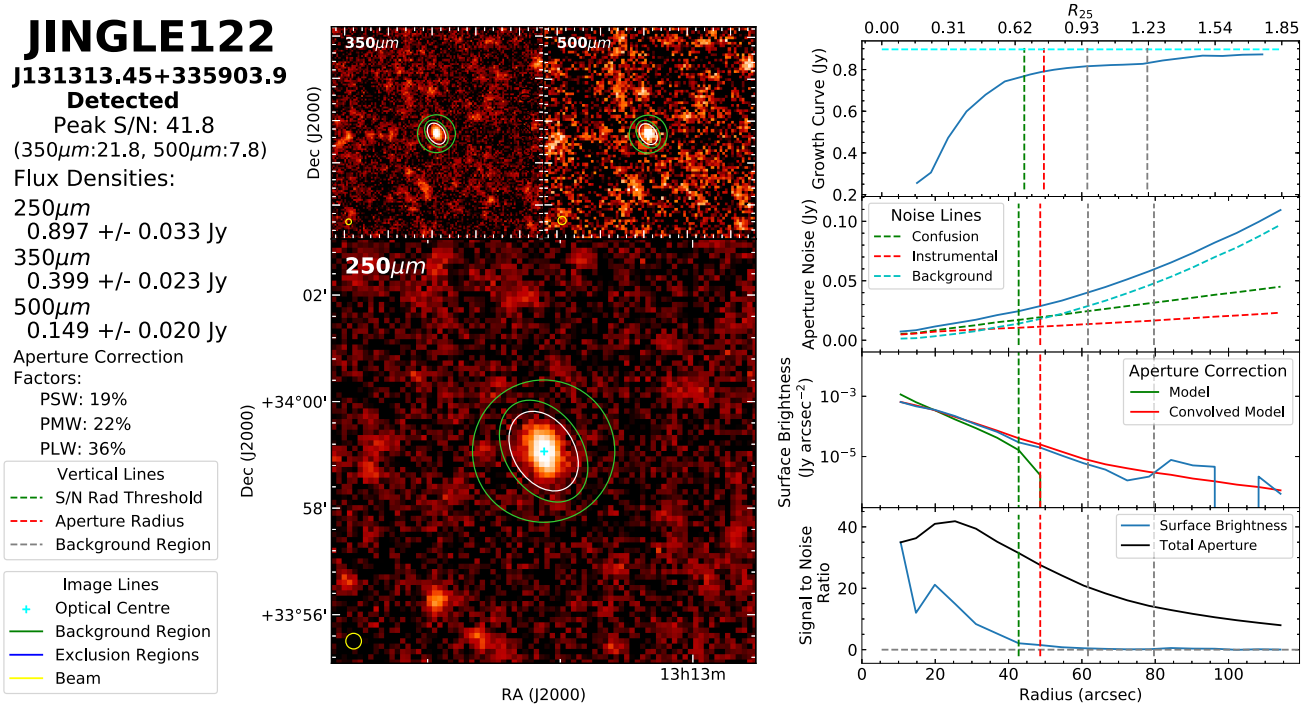

Figure 5. The diagnostic image produced by the photometry pipeline for JINGLE 122 for the SPIRE wavelengths. The images in the centre show the aperture (white) and the background region used (green) on the images, as well as the optical centre (cyan cross) and FWHM beam size in yellow. If objects were to be excluded from the analysis they would be shown in blue. On the right of the graphic we have various curves which vary with radius; the top plot shows the growth curve (horizontal cyan line is the flux measurement), the second from top plot shows how the aperture noise grows as function of the different noise sources, third from top is the surface brightness profile (blue) with the exponential aperture correction models shown (green model, red convolved with beam), and the bottom plot shows the signal-to-noise of the surface brightness profile (blue) and total aperture (black). On all the radial plots the vertical green line shows where the surface brightness profile crosses a signal-to-noise of 2 and the red line is the radius of the aperture. The vertical grey lines show the radii of the background region. Finally on the left the peak signal-to-noise, fluxes, and aperture corrections are listed.

pixels within that region contaminated by the late-type galaxy were replaced with a sigma-clipped mean of the map, and the resulting image then used to perform the usual aperture flux extraction method.

4.2 Point source extraction

Several of our sources are compact enough they are well described by a point source in the FIR wavelengths from PACS to SCUBA-2. By identifying point sources we can use extraction techniques

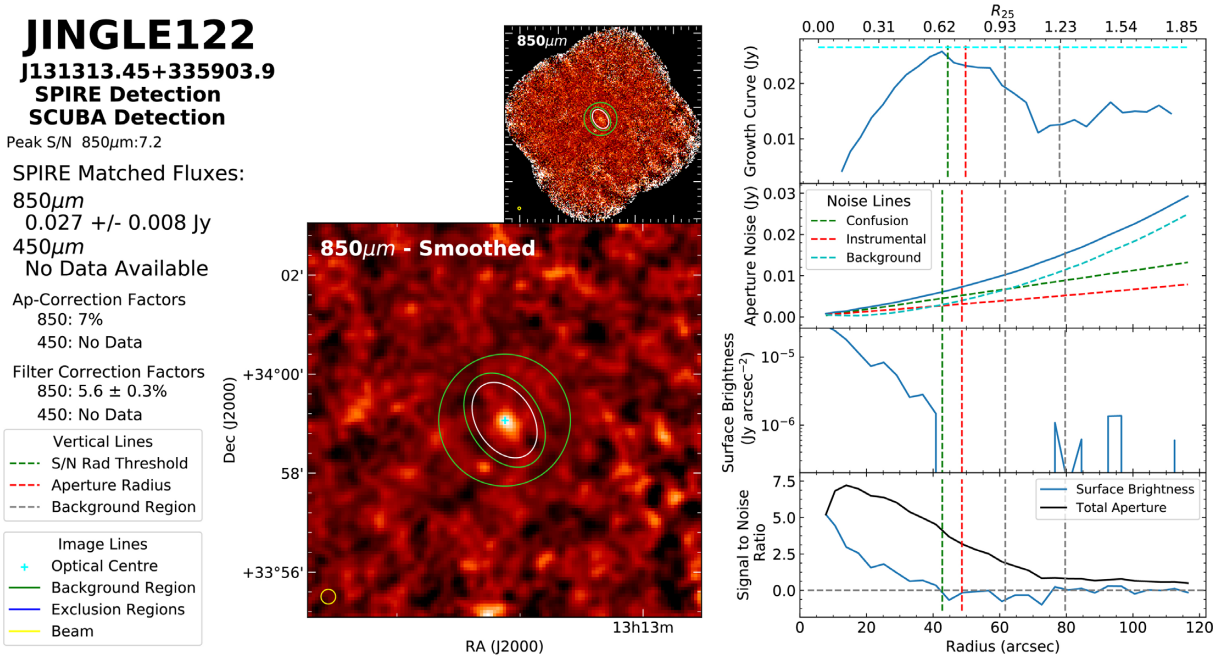

Figure 6. Same as Fig. 5, except now applied to SCUBA-2. Unlike the SPIRE 250 μm figure the aperture is matched to the SPIRE band (rather than derived from the image).

optimized to recover flux densities using the PSF as a prior, rather than relying on aperture photometry. This improves both the flux estimate and the significance of the detection (particularly in the SCUBA-2 bands). For SPIRE to fit a point source the images are firstly converted into units of Jy beam^{-1} and then NEBULISER is run over the maps to remove any emission on scales greater than 3 arcmin. We then fit a radially averaged PSF in each band, using a model grid based on five times smaller pixels than the original pixel size to minimize the effect of pixelization. For the SPIRE 250 μm we allow the central position to vary by up to 6 arcsec compared to the optical centre, while for other bands the central position is locked to the SPIRE 250 μm position. The largest offset was found to be 3.3 arcsec with most offsets substantially smaller. For the SPIRE bands the uncertainty in the flux is measured using the uncertainties measured in the fit combined with the confusion noise (as given in Table 1). An example of the point source extraction applied to a SPIRE image is shown in Fig. 7.

To decide whether our candidate galaxies can be reasonably approximated by point sources as well as a visual inspection, we run the residual images through our aperture photometry code as described in Section 4.1. If the residual signal in the aperture at 250 μm has a signal-to-noise <2.5 then we use the point source procedure. From our sample of 193 galaxies, 42 meet our criteria to be considered point-like.

For the SCUBA-2 images we first apply the 'match-filter' ORAC-DR recipe which optimizes SCUBA-2 maps for point source extraction. Effectively the recipe subtracts a Gaussian smoothed version of the map and convolves the map with the SCUBA-2 PSF. We then fit the matched-filter PSF characterized by Geach et al. (2017), with the source centre fixed to the SPIRE position. However, as the matched-filtering convolves the image the noise of each pixel can no longer be considered independent. We therefore perform a Monte Carlo simulation where for every pixel in the raw map we scale a normally distributed random number to account for the instrumental noise in the pixel and add it to the map. The same matched-filtering and point source extraction is performed to the new map and the whole process repeated 100 times. The uncertainty in the flux is then estimated based on the distribution of extracted fluxes. Note, that despite the slightly higher angular resolution of the JCMT at 850 μm than SPIRE at 250 μm, with the smoothing action of the matched-filter these sources should be well represented by a point source).

Three candidate point-galaxies that narrowly failed our criteria (JINGLE 162, 182, and 192) at SCUBA-2 850 μm, were found to have higher flux measurements when using the point source measurement, compared to the aperture photometry method, due to noise in the aperture. For these three galaxies we therefore report the point source flux (this again is helped by the smoothing action of the matched-filter).

The *H*-ATLAS team recommends for PACS data that apertures of radius 11.4 and 13.7 arcsec are used for the extraction of point sources (Valiante et al. 2016; Smith et al. 2017), due to variations of the beam shape. As the WISE data are of similar or better resolution we use the same 11.4 arcsec radius for the W1–W3 bands and 13.7 arcsec radius aperture for the W4 band. Whether the point source extraction method is used in either the SPIRE or the SCUBA-2 850 μm bands is specified in the flux-density catalogue table available in the supplementary materials or on the JINGLE data release page[2].

4.3 Simulations

As mentioned in Section 3.1, the SCUBA-2 pipeline relies on high-pass filtering, and while we have tried to minimize the effect when creating a map there could be some residual flux attenuation. To try to correct for this effect for each object we run a simulation where we inject a model of the source into the raw instrumental data of JINGLE observations that appear to have no signal (although to avoid any bias we avoid the location of the target galaxy). From our observations observed up to 2016 December we identified 12

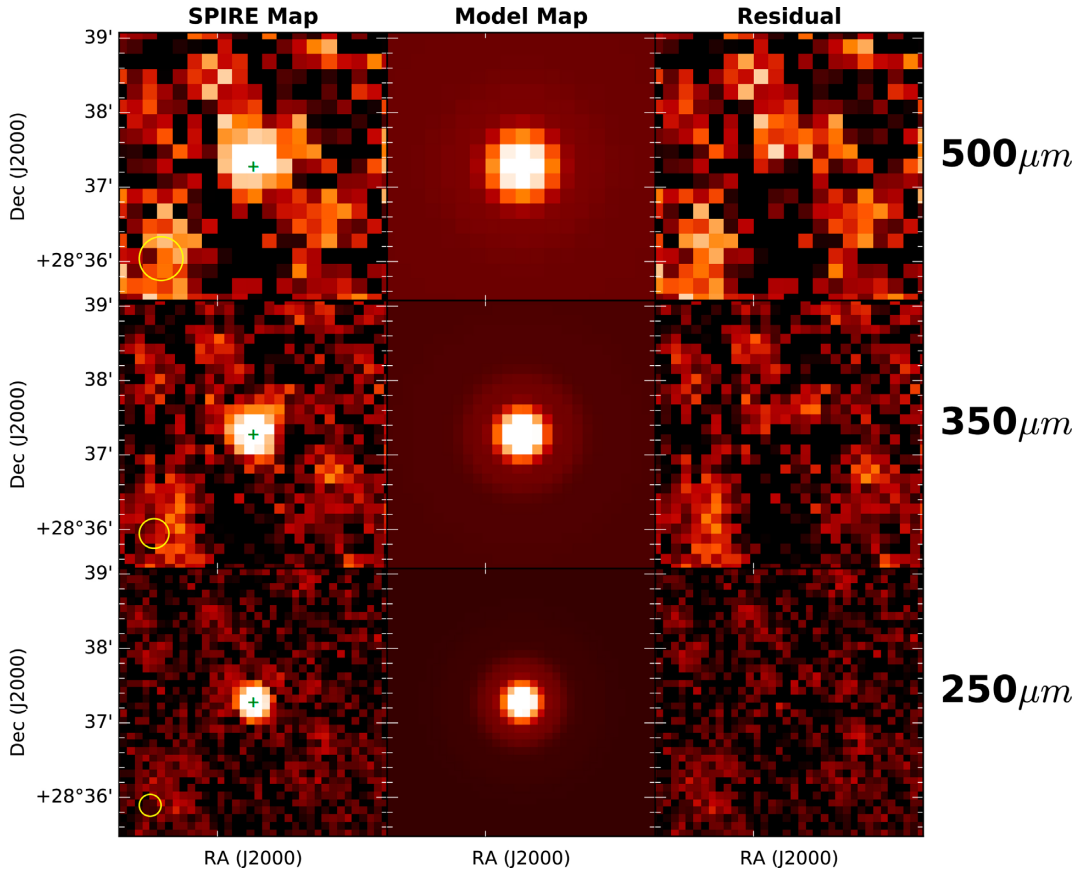

Figure 7. An example of the point source fitting method for JINGLE 33 in the SPIRE wavelengths. The grid of images show the SPIRE maps (left column), the point source model images (middle column), and the residual images after the point source is subtracted (right column) for the 250, 350, and 500 μm bands. On the SPIRE maps the optical centre is shown by the cyan cross, the fitted centre by the green cross (in this example the two overlap so only the green cross is visible) and the beam FWHM in yellow.

target regions that could be used for this purpose. The raw data with the injected source is then processed with the same map-making procedure as for the real data (including same mask size and configuration). To minimize the effect of the noise on our correction, we also re-run the map-making but with no model source injected using the same mask. This blank map is then subtracted from the map with the injected source and estimates of both the aperture and filter corrections are calculated.

To make the model that is injected into the raw data we take the exponential models used to find the aperture corrections in the SPIRE data (see Section 4.1), these are then convolved with the SCUBA-2 beam and the flux adjusted to match our predicted 850 μm flux. The model source is then converted into pW so it matches the units of the instrumental timelines. For each JINGLE target we inject the galaxy into three different blank fields chosen to have the closest sensitivity to our target observation (estimated in the central region of the instrumental uncertainty map). The model source to be injected is adjusted so the signal-to-noise ratio is the same for the injected source as expected in the real map (from the predicted flux-density). The centre and orientation of the injected source is chosen randomly, but the distance from the centre of the image is limited to be within 2 arcmin so we are not affected by the noisy regions at the edges of the map. The random location is not allowed to overlap with the intended target of the 'blank' data. The size of the mask used is identical to that applied to the reduction of the target observation.

For galaxies that we assume are point-like the correction factor (this correction also accounts for any systematic from the matched-filtering and flux extraction process we have not accounted for) has an average value of 1.135 with a narrow distribution (minimum factor 1.121 and maximum 1.158). For extended galaxies the average filter correction is lower at 1.045, but has a much larger range from 1.006 to 1.139. These corrections have been applied to all fluxes provided in the catalogue.

4.4 Catalogue statistics

At 250 μm 191 of the 193 galaxies in the JINGLE sample are easily detected ($>5\sigma$) by SPIRE with most objects having peak signal-to-noise ratios between 10–50 (the high fraction is not surprising as galaxies were included in our sample based on a preliminary *H*-ATLAS catalogue). The two notable exceptions are JINGLE 62 and JINGLE 130, neither of which are listed in the release version of the *H*-ATLAS DR2 catalogue (Maddox et al. 2018). From our measurements JINGLE 130 is identified with a peak signal-to-noise ratio of 4.5 and is identified as a point-like source. We therefore follow the same procedures as galaxies detected with signal-to-noise ratios >5. JINGLE 62 is fainter than JINGLE 130 and has a significance far below 3.0σ, we therefore just report an upper-limit to the flux for this source across all the wavebands, using an elliptical aperture with semimajor axis equal to R_{25} (this size was chosen to match findings of the HRS, Ciesla et al. 2012; Smith et al. 2012a).

Table 2. Sample detection statistics.

Instrument	Band	Peak S/N		Total S/N	
		$\geq 5\sigma$	$\geq 3\sigma$	$\geq 5\sigma$	$\geq 3\sigma$
SPIRE	250 μm	191/193	192/193	191/193	192/193
	350 μm	186/193	190/193	185/193	190/193
	500 μm	93/193	138/193	79/193	132/193
PACS	100 μm	177/190	181/190	157/190	174/190
	160 μm	182/190	187/190	177/190	185/190
WISE	3.4 μm	192/193	192/193	189/193	189/193
	4.6 μm	192/193	192/193	189/193	189/193
	12 μm	192/193	192/193	192/193	192/193
	22 μm	188/193	192/193	186/193	188/193
SCUBA-2	850 μm	62/193	126/193	30/193	83/193

Notes. The total number of objects in the PACS sample is 190 instead of the 193 for SPIRE, WISE, and SCUBA-2, as 3 galaxies were not covered by PACS imaging due to the 22 arcmin offset between the PACS and SPIRE cameras on the *Herschel* focal plane.

Table 2 provides an indication of our detection rates across the different bands, by giving the number of objects with signal-to-noise ratios greater than 5 or 3. The table is split by peak signal-to-noise ratio, which is the aperture that gives the highest signal-to-noise, while the total signal-to-noise is the measurement on the total aperture. The peak measurement is more analogous to a detection statistic while the total aperture shows the ability to measure the total flux of an object (for point sources the peak and total S/N are the same). As outlined in Section 4, we use the SPIRE 250 μm data to define our apertures, so that we get aperture matched fluxes (or point source estimates) across all wavebands even if the signal-to-noise ratio is significantly lower in other bands.

Table 2 shows that we have secure WISE and SPIRE 250/350 μm detections for almost every object in our sample and over 82 per cent with PACS coverage (with total S/N > 5). At SPIRE 500 μm as we move down the Rayleigh–Jeans tail the number of galaxies detected drops to 48 per cent at 5σ, and 41 per cent have total fluxes with signal-to-noise ratios greater than 5. The JINGLE SCUBA-2 850 μm of course is more challenging due to the intrinsically fainter emission of local galaxies in this waveband and the effects of the atmosphere, but we do detect 126 of our 193 (65 per cent) at a level of $>3\sigma$, and have 83 (43 per cent) galaxies where the total signal-to-noise of the flux measurement is greater than 3. However, galaxies with lower signal-to-noise can still be useful to constrain the dust properties of an object. The distribution of the peak and total aperture signal-to-noise measurements for our SCUBA-2 sample is shown in Fig. 8.

The complete table of flux-densities in the WISE, PACS, SPIRE, and the SCUBA-2 850 μm bands is available in the supplementary materials and on the JINGLE data release page[2]. The python scripts used to perform the photometry are available online.[5]

5 CO(3–2) CONTAMINATION

The CO(J = 3–2) emission line at 867.6 μm (354.796 GHz) falls within the bandpass filter for the 850 μm SCUBA-2 band for all the galaxies in the JINGLE sample ($z < 0.05$); leading to potentially significant contamination of the continuum flux (Drabek et al. 2012). In order to correct for this contamination, we need to

[5]https://github.com/mwls/Public-Scripts

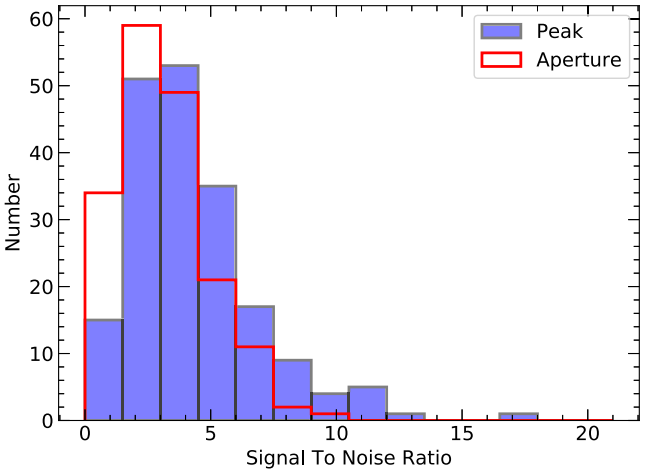

Figure 8. A histogram of the signal-to-noise ratio values for the flux measurements of JINGLE galaxies at the SCUBA-2 850 μm wavelength. The blue filled histogram is the peak signal-to-noise (see text) while the open red histogram is the signal-to-noise of the SPIRE matched aperture.

estimate the strength of the CO(J = 3–2) emission line. For the JINGLE galaxies we do not have CO(J = 3–2) observations, but we have predictions of the CO(J = 1–0) luminosity from Xiao et al., in preparation (Paper III). In this paper, they show that these predictions are in good agreement with the CO line luminosities measured for a sub-sample of JINGLE galaxies. The CO(J = 3–2) line luminosity can be estimated from the CO(J = 1–0) transition, assuming an excitation line ratio $r_{31} = L'_{\rm CO(J=3-2)}/L'_{\rm CO(J=1-0)}$.

To estimate the ratio r_{31} for the JINGLE galaxies, we studied a sample of ∼20 galaxies from the COLD GASS survey (Saintonge et al. 2011) which allowed us to measure r_{31} in a redshift range similar to that of the JINGLE survey. The galaxies of this sample also have stellar masses, specific star-formation rates (SSFR) and star-formation efficiencies [SFE = SFR / M(H_2)] comparable to the JINGLE sample. We found a mean value of $r_{31} = 0.53 \pm 0.05$. This value is consistent with observations of low-redshift galaxies (average $r_{31} = 0.6 - 0.7$, Yao et al. 2003; Mao et al. 2010; Papadopoulos et al. 2012) and intermediate redshift ($z \sim 0.3$) star-forming galaxies (average $r_{31} = 0.46 \pm 0.07$, Bauermeister et al. 2013). Therefore we decided to use the constant value $r_{31} = 0.5$.

We converted the obtained line luminosity $L'_{\rm CO(J=3-2)}$ into line intensity $I_{\rm CO(J=3-2)} = \int T_{\rm MB} {\rm d}v$ in (K km s^{-1}) using equation (2) from Solomon et al. (1997):

$$I_{\rm CO(J=3-2)} = \frac{L'_{\rm CO(J=3-2)}}{23.5 \times \Omega_{\rm b} D_L^2 (1+z)^{-3}} \quad (1)$$

where $L'_{\rm CO(J=3-2)}$ is in units of (K km s^{-1} pc^2), $\Omega_{\rm b}$ is the telescope beam area in $arcsec^2$ and D_L is the luminosity distance in Mpc. We assume that the sizes of our galaxies are comparable to the size of the SCUBA-2 beam (13.5' FWHM), and use $\Omega_{\rm b} = \pi(13.5/2)^2$ $arcsec^2$.

To convert the line intensity from line units (K km s^{-1}) to SCUBA-2 850 μm continuum flux, we used the conversion factor C defined by Drabek et al. (2012) as:

$$C = \frac{F_\nu}{\int T_{\rm MB} {\rm d}v} = \frac{2k\nu^3}{c^3} \frac{g(\nu)}{\int g(\nu) {\rm d}\nu} \Omega_{\rm B}, \quad (2)$$

where C has the units mJy $beam^{-1}$ per K km s^{-1}. F_ν is the line flux, $\int T_{\rm MB} {\rm d}v$ is the integrated main-beam temperature, k is the Boltzmann constant, $g(\nu)$ is the transmission at the frequency ν of

the 850 μm filter multiplied by the atmospheric transmission, and Ω_B is the telescope beam area.

The C factor that converts the line intensity into SCUBA-2 continuum flux depends on the atmospheric transmission. We used the updated prescription for the C conversion factor from Parsons et al. (2018), which provides the C factor as a function of the precipitable water vapour (PWV). The main differences from the prescription by Drabek et al. (2012) are that they used an updated main-beam FWHM of 13.0 arcsec with a relative amplitude of 0.98, and that they include a correction for the secondary beam component, which has a relative amplitude of 0.02 (Dempsey et al. 2013). The C factor as a function of PWV is defined as:

$$C = 0.574 + 0.1151 \times \mathrm{PWV} - 0.0485 \times \mathrm{PWV}^2 + 0.0109 \times \mathrm{PWV}^3 - 0.000856 \times \mathrm{PWV}^4 \ \mathrm{mJy\ beam^{-1}/K\ km\ s^{-1}}, \quad (3)$$

where the PWV is related to the sky opacity at 225 GHz ($\tau_{225\mathrm{GHz}}$) as $\mathrm{PWV} = (\tau_{225\mathrm{GHz}} - 0.017)/0.04$ mm. The C factor for our sample varies in the range 0.63–0.75 (mJy beam^{-1} per K km s^{-1}). The C factors are calculated at the rest-frame frequency of CO(J = 3–2). To account for the different transmission at the observed frequency of CO(J = 3–2), we applied the following correction:

$$C_{\mathrm{obs}} = \frac{1}{(1+z)^3} \times \frac{g(\nu_{\mathrm{obs}})}{g(\nu_{\mathrm{rest}})} \times C, \quad (4)$$

where ν_{rest} is the CO(J = 3–2) rest-frame frequency and $\nu_{\mathrm{obs}} = \nu_{\mathrm{rest}}/(1+z)$ is the CO(J = 3–2) observed frequency. For each JINGLE observation we average the $\tau_{225\,\mathrm{GHz}}$ values for each observation and then calculate the correction.

Thus, the CO(J = 3–2) flux contamination in [mJy beam^{-1}] is:

$$F_{\mathrm{CO(3-2)}} = \int T_{\mathrm{MB}} \mathrm{d}v \times C_{\mathrm{obs}}. \quad (5)$$

The CO(J = 3–2) flux contamination is in the range 0.7–41.2 per cent of our predicted 850 μm values with a mean contamination of 10.1 per cent. For the vast majority of sources (78 per cent) the correction is less than 15 per cent of the predicted 850 μm flux density, and 91 per cent of sources have corrections less than 20 per cent of the predicted 850 μm flux density. The SCUBA-2 flux estimated contamination is provided in the main catalogue table available in the Supplementary Materials. After correcting for the CO (J = 3 − 2) flux contamination 73 of our targets have aperture fluxes with a signal-to-noise greater than 3.

6 RESULTS AND DISCUSSION

6.1 Comparison of the predicted and observed SCUBA-2 fluxes

In this section, we compare the observed SCUBA-2 850 μm fluxes with predictions from fitting the FIR SED using our *Herschel* data in the wavelength range 100–500 μm. We used a single modified blackbody model (SMBB) defined as (Hildebrand 1983):

$$F_\lambda = \frac{M_{\mathrm{dust}}}{D^2} \kappa_\lambda B_\lambda(T_{\mathrm{dust}}), \quad (6)$$

where M_{dust} is the dust mass in the galaxy, D is the distance of the galaxy, and $B_\lambda(T_{\mathrm{dust}})$ is the Planck function for the emission of a blackbody with a dust temperature T_{dust}. The dust mass absorption coefficient κ varies as a function of wavelength:

$$\kappa_\lambda = \kappa_0 \left(\frac{\lambda_0}{\lambda}\right)^\beta, \quad (7)$$

where κ_0 is the reference dust mass absorption coefficient. We use a constant value $\kappa_0 = 0.051\,\mathrm{m^2\,kg^{-1}}$ at 500 μm from Clark et al. (2016). We assume a fixed emissivity index $\beta = 2$ to have conservative estimates of the flux, since β is typically in the range 1.5–2.0 (e.g. Boselli et al. 2012; Galametz et al. 2012; Smith et al. 2012b; Clemens et al. 2013; Cortese et al. 2014). We fit the model to the *Herschel* fluxes (100, 160, 250, 350, and 500 μm), using a Bayesian non-hierarchical method implemented using the MCMC code `emcee` (Goodman & Weare 2010; Foreman-Mackey et al. 2013), and assuming that the noise is normally distributed. For details about the fitting procedure see Lamperti et al., in preparation. The predicted spectra in the 850 μm band were convolved with the filter transmission curve of the SCUBA-2 band, before comparing them with the observed fluxes.

Fig. 9 shows the comparison between the predicted and observed 850 μm fluxes. As the JINGLE observations were individually tuned to reach a fixed detection threshold (rather than a fixed sensitivity), galaxies with a higher measured flux density than predicted tend to be detections, while those with lower than predicted flux density do not reach our detection criteria. While the kernel-density estimator (KDE) graph (right-hand panel Fig. 9), peaks in agreement with our predictions, generally there is a large scatter. For the majority of objects (∼75 per cent) the scatter could be explained simply due to the uncertainty in the flux measurement. However, the distribution is wider than you would expect from the uncertainties (both above and below our predictions). More galaxies (110 versus 82) show an excess of the observed fluxes (i.e. they are higher than the predictions), meaning that for those galaxies the slope of the SED in the sub-millimeter is shallower. The most likely explanation is that their dust SED should be modelled with a lower β value, either due to the intrinsic dust properties or from multiple dust temperature components along the line of sight. Several studies have found β varying between 0.5–2.5 on global scales (e.g. Boselli et al. 2012; Galametz et al. 2012; Clemens et al. 2013; Cortese et al. 2014) and within a galaxy (Smith et al. 2012b; Kirkpatrick et al. 2014; Tabatabaei et al. 2014). We will investigate this further in subsequent sections.

There are also galaxies for which the observed flux is lower than the predicted flux. Our predictions could overestimate the true 850 μm flux density if the dust emissivity index could be greater than 2 (e.g. Lis et al. 1998; Meny et al. 2007; Smith et al. 2012b), or if we have overestimated the CO(J = 3–2) contribution for these galaxies. For JINGLE we estimated the CO(J = 3–2) contribution from the predicted CO(J = 1–0) luminosity, using a constant line excitation correction factor $r_{31} = L_{\mathrm{CO(3-2)}}/L_{\mathrm{CO(1-0)}} = 0.5$, but this factor is known to vary in the range 0.1–1.9 (Mauersberger et al. 1999; Yao et al. 2003; Mao et al. 2010). Assuming an extreme value of $r_{31} = 0.1$, the CO(J = 3–2) contribution will be a factor of five lower. The estimated CO contribution is lower than 30 per cent of the observed flux for 95 per cent of our sample. Thus an overestimation of r_{31} can only account for a deficit of ∼25 per cent of the observed flux with respect to the predictions. As shown in Fig. 9, the observed deficit can be as large as the predicted flux density, therefore the CO(J = 3–2) contribution is not sufficient to explain the deficit.

6.2 Far-infrared colours

In this section, we investigate how FIR/sub-mm colours vary with each other and compare with the predictions of modified blackbody models. We define a FIR/sub-mm colour as the ratio of two flux-densities at wavelengths in the range 100–850 μm. We investigate a selection of colour ratios that sample different regions of the FIR spectrum. For example the ratio at smaller wavelengths like

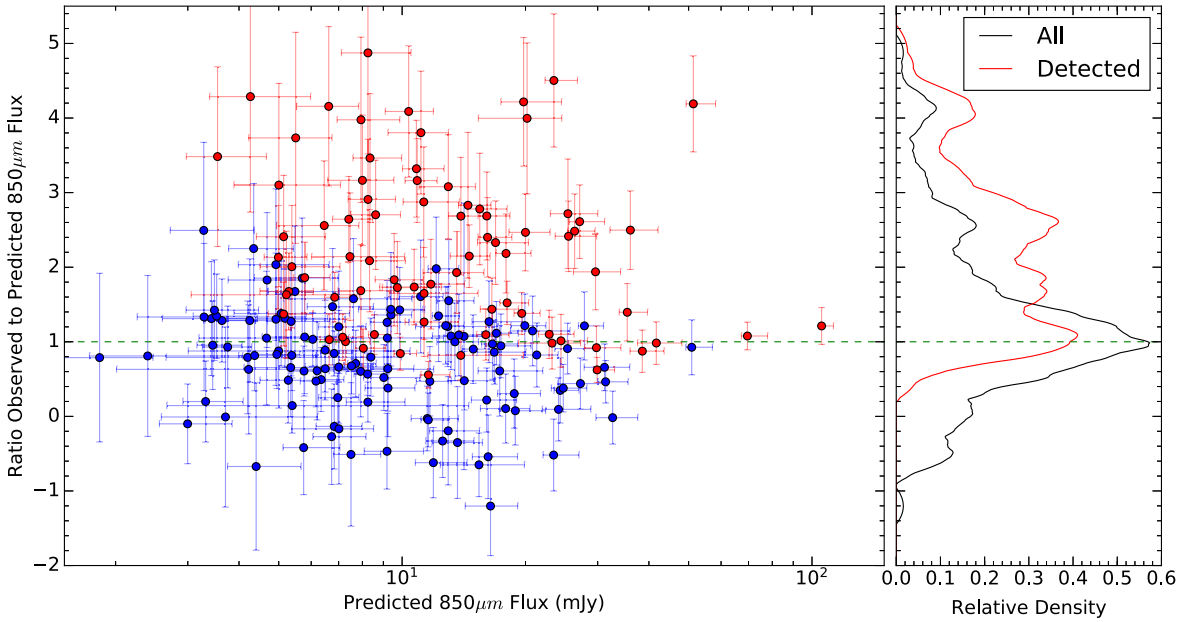

Figure 9. The left-hand panel shows the ratio of the observed flux to the predicted 850 μm flux versus the predicted flux. The 850 μm flux predictions are based on a fit of a single modified black-body to the *Herschel* bands with a fixed emissivity index $\beta = 2$. Objects that have measured fluxes with signal-to-noise ratios greater than 3 are shown by the red points, and all other objects in blue. The horizontal green dashed line is where the ratio of observed to predicted 850 μm flux is 1. The right-hand panel shows the KDE of the ratio of observed to predicted 850 μm flux for all objects (black line) and those with measured flux ratios with S/N > 3 (red line).

F_{100}/F_{160}, and F_{100}/F_{250} should be more sensitive to temperature variations of the dust. Colour-ratios including flux densities at longer wavelengths F_{160}/F_{500}, F_{250}/F_{500}, and F_{160}/F_{850} should be more sensitive to changes in the dust emissivity index (β).

Fig. 10 shows a grid of the FIR/sub-mm colour ratios (similar to those derived for the HRS in Boselli et al. 2012 and Cortese et al. 2014), the best correlation between FIR colours is seen for indicators that trace the dust emissivity index (i.e. longer wavelengths). The highest correlation is seen between the F_{250}/F_{850} and F_{160}/F_{850}, with the Spearman rank coefficient (ρ) equal to 0.96. This shows the advantage of having the longer 850 μm SCUBA-2 data to constrain the Rayleigh–Jeans tail, as using only the SPIRE wavelengths $\rho = 0.80$, for the F_{250}/F_{500} and F_{250}/F_{350} colour ratio. The two shorter colour-ratios (F_{100}/F_{250} and F_{100}/F_{160}) also show a very good correlation ($\rho = 0.77$), probably as both are indicative of dust temperature.

Similar correlations to those shown in Fig. 10 were found by Boselli et al. (2012), for the HRS (Boselli et al. 2010a), with their best correlation ($\rho = 0.98$) between F_{250}/F_{500} and F_{250}/F_{350}. Overall, the *Herschel* Reference Survey predominately had stronger correlations than we find for JINGLE, although this could be explained due to the HRS targeting local galaxies with significantly higher global flux estimates, and deeper observations than *H*-ATLAS.

In Fig. 11, we show the four colour-ratios from Fig. 10 with the highest Spearman's rank correlation, including the uncertainties for each data point. For the colour-ratios not including 850 μm we overplot objects from the HRS in grey (Boselli et al. 2012; Cortese et al. 2014). Given the large difference in selection (the HRS is a local *K*-band selected sample) compared to JINGLE, the distribution of the detected HRS galaxies in the colour ratio plots appears very similar to that of JINGLE, suggesting the dust properties of both samples are broadly similar. This is possibly due to the similar stellar masses of the samples, although the specific SFR is quite different (see JINGLE Paper IV, de Looze et al., in preparation). The red, green, and orange lines in Fig. 11 show the line produced for an SMBB with a $\beta = 2$, $\beta = 1.5$, and $\beta = 1$ over a temperature range of 15–30 K, respectively. The distribution of points in the top-left panel is dominated by the temperature of the dust as shown by the similarity of the two blackbody lines. The blackbody lines show that a temperature range of 15–30 K is sufficient to explain the vast majority of JINGLE and HRS objects (in agreement with JINGLE Paper V, Lamperti et al., in preparation). The top-right and bottom-left panels show the difficulty in making estimates of the dust emissivity index from *Herschel* data alone where both modified blackbody models with $\beta = 1.5$ and 2 lie within the scatter of the data for the sample. The bottom-right panel which shows the F_{250}/F_{850} versus F_{160}/F_{850} shows the extra discrimination between models that the longer wavelength data provides, with the objects at high F_{250}/F_{850} and F_{160}/F_{850} appearing to lie on the $\beta = 2$ line, while surprisingly the majority of objects appear to fall below the $\beta = 1$ line.

To test the significance of our colour-plots to distinguish between the dust models, for each data point we calculated the smallest 'normalized' distance (i.e. the smallest distance between the models divided by the uncertainties). If the model is an accurate description of the data, the distribution of the normalized distances should be a normal distribution. We then use the Anderson–Darling test[6] to test the null hypothesis that our distribution is drawn from the normal distribution. The F_{160}/F_{500} versus F_{100}/F_{250} reject the $\beta = 1.5$ and $\beta = 2.0$ models as the test statistic of 1.11 and 4.64 is above the critical level of 1.06 and so the probability of our data being drawn from the distribution is < 1 per cent. The F_{250}/F_{850} versus F_{160}/F_{850} also rejects the $\beta = 2.0$ model with a probability <1 per cent, but

[6]We use the scipy implementation of the Anderson–Darling test (Jones et al. 2001).

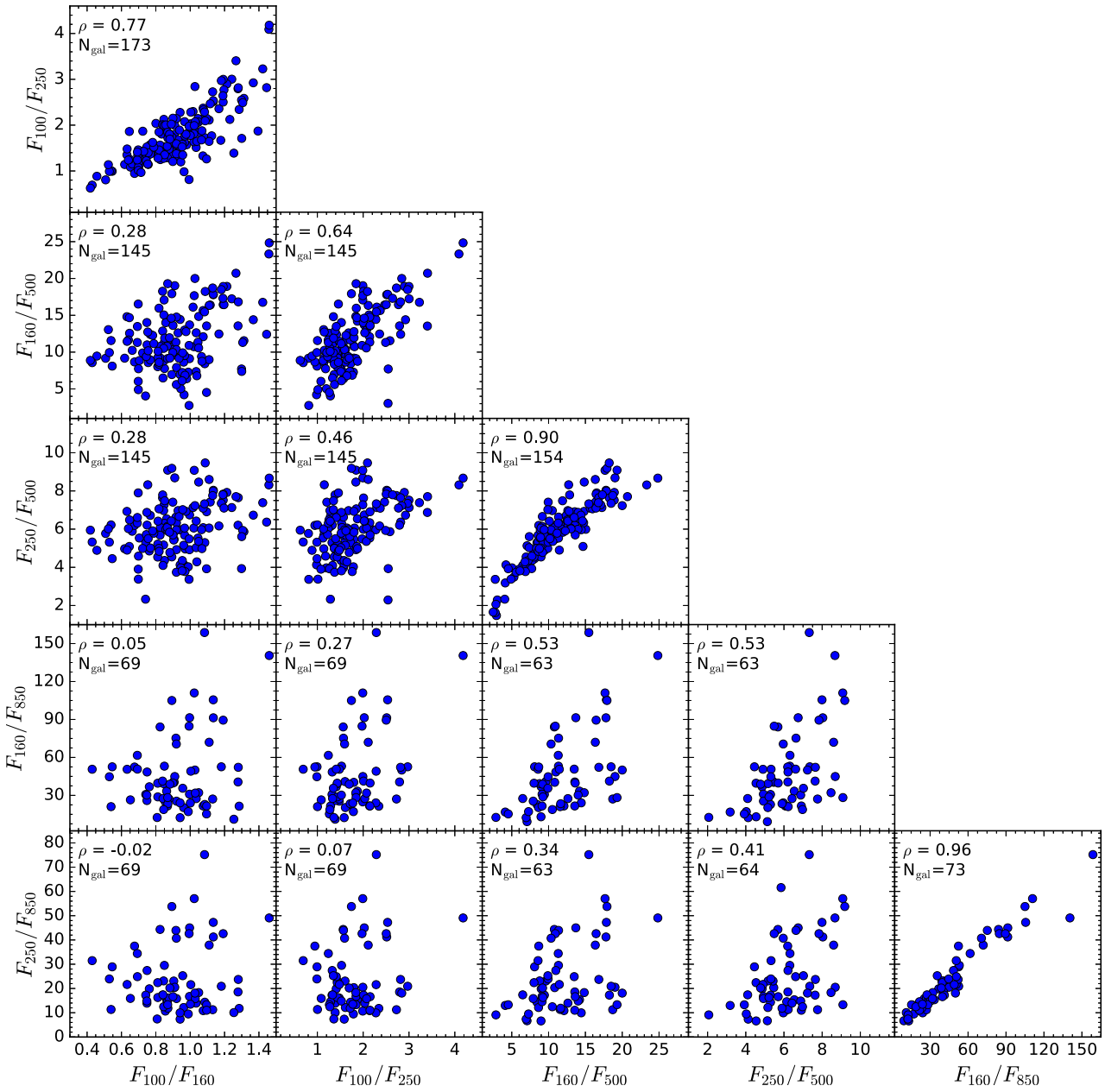

Figure 10. Far-infrared/sub-mm colour–colour plots for selected colours, where each colour is the ratio of two flux-densitites in the wavelength range 100–850 μm. Galaxies are only included if each flux-density in the panel has a signal-to-noise ratio greater than 3. The Spearman's rank correlation coefficient (ρ), and the number of galaxies in each panel is given in the top left corner of each panel.

is not as significant for $\beta = 1.5$ with ∼5 per cent probability the data are drawn from the distribution. However, the statistics with F_{850} are likely to be an underestimate of the model rejection, as a plot of the residuals (i.e. data – model), shows a strong correlation ($\rho > 0.6$) and significant (p-values $<5 \times 10^{-9}$) as measured by the Spearman rank coefficient.

Our results confirm the findings of Boselli et al. (2012) that an SMBB model with a constant β cannot explain the distribution of points in both the *Herschel* wavelengths (i.e. the top-right panel in Fig. 11), and the SCUBA-2 850 μm data. While both single β models are rejected by the *Herschel* data, values between 1.5 and 2.0 would explain the majority of data points. The bottom-left panel of Fig. 11, shows many colour-ratios lie below the $\beta = 1.5$ line. It is possible to explain some of the systematic shift in the bottom-right panel by having an extreme calibration uncertainty for PACS and SPIRE, or by requiring a large colour correction. However, a large calibration shift of the *Herschel* data would lead to worse agreement in the other panels, and can only partly resolve the offset. The colour corrections for both PACS and SPIRE are small (≈3 per cent) for a typical galaxy spectrum, and cannot resolve the offset. A potential solution is that a single dust component may not be a good model for a galaxy's spectrum and multiple temperatures along the line-of-sight are required. Clark et al. (2015) performed an investigation of a blind dust survey of nearby galaxies ($15 < D < 46$ Mpc) using *H*-ATLAS (the HAPLESS sample), and so has similar detection criteria to that of JINGLE. For their sample they found that they

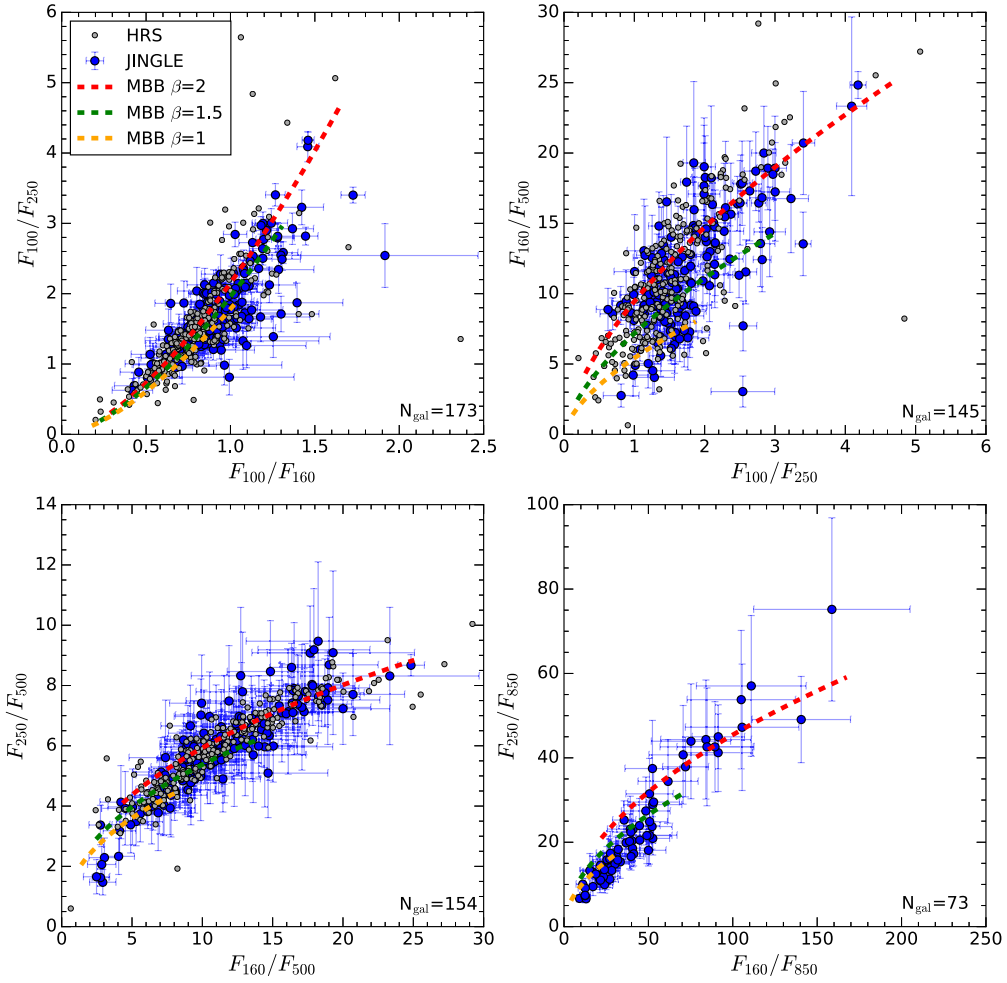

Figure 11. The four far-infrared/sub-mm colour–colour plots from Fig. 10 with the strongest correlations. The blue points with error bars are points with a signal-to-noise ratio greater than 3. The grey dots show the position of detected galaxies from the HRS with no photometry flags in the catalogue. The red, green, and orange lines are the flux-density ratios of a single-modified blackbody between a temperature of 15 and 30 K with a β of 2, 1.5, and 1, respectively.

required a two-temperature component distribution to adequately describe their FIR fluxes, with many galaxies in their sample having an ∼9–15 K cold component. Using their best-fitting parameters, a couple of the objects overlap with the extreme bottom left of the JINGLE distribution in a plot of F_{250}/F_{850} versus F_{160}/F_{850}, the vast majority of HAPLESS galaxies lie between our SMBB with $\beta = 1.5$ and $\beta = 2.0$. However, the HAPLESS SED fits were performed assuming a $\beta = 2$ in the 60–500 μm wavelength range, and so extrapolating their models may not give the true HAPLESS flux.

A broken emissivity modified-blackbody model where the emissivity law changes β value at a break wavelength (where λ_{break} >175 μm, see Li & Draine 2001; Gordon et al. 2014, for more details of the model), can be used to provide a better fit. In particular the cluster of objects with low F_{250}/F_{850} versus F_{160}/F_{850} values in Fig. 11 could be explained, although the break wavelength is at longer wavelengths (e.g. ≈500 μm). Even if such a model could explain the excess at 850 μm, it is clear one dust model cannot explain the entire distribution of JINGLE galaxies.

Another possibility is that our signal-to-noise cut of 3 is artificially selecting galaxies that have been boosted to high-850 μm flux densities. However, lowering the signal-to-noise cut to 2 results in the same observed discrepancy.

In the next section, we avoid this issue as for each galaxy we use the results of fitting a modified blackbody model to each galaxy in JINGLE, as we have performed aperture matched photometry across all bands, even a low signal-to-noise 850μm measurement can be useful to constrain the fitted parameters.

6.3 Far-infrared colours as indicators of dust temperature and emissivity

We investigate the effect of including the 850 μm flux on the measurement of the effective emissivity index β. We perform the SED fitting with β as a free parameter, and we compared β measured from the fit with and without the 850 μm flux (Fig. 12). The points are scattered predominantly around the one-to-one relation. The largest discrepancies are for galaxies that have β values <0 when obtained using *Herschel* data only, presumably due to low signal-to-noise in the longer SPIRE wavelengths. When our 850 μm measurements are included all but one of these objects have values above $\beta = 0$ (values of β below 0 are not physically possible).

The KDE panels in Fig. 12 show the distribution of β's measured for the majority of objects is similar before and after the 850 μm is included. However, 48 per cent of the sample have estimates of β below 1.5, which may be an indication of a submm excess, (i.e.

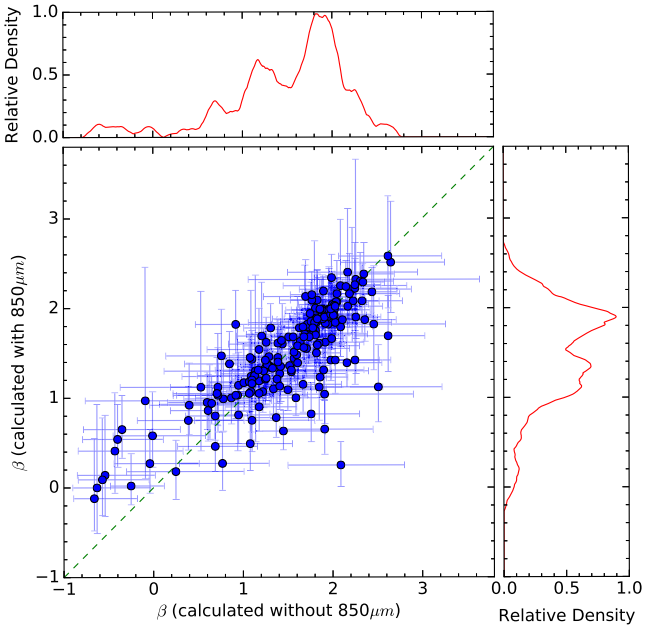

Figure 12. Comparison of the emissivity index β measured from the *Herschel* bands and measured with the additional SCUBA-2 850 μm flux point. The green dashed line shows the one-to-one relation (i.e. when the two estimates agree). The top and right-hand panels show the KDE for each set of β points, which clearly show how the 850 μm flux changes the distribution of values measured.

an excess emission at wavelengths ≥500 μm with respect to what models would predict from the 100–350 μm wavelength range). Such an excess has been observed in dwarf galaxies (Lisenfeld et al. 2002; Galliano et al. 2003), in late-type galaxies (Dumke, Krause & Wielebinski 2004; Bendo et al. 2006; Galametz et al. 2009; Rela no et al. 2018), as well as in the Magellanic Clouds (Bot et al. 2010; Israel et al. 2010; Planck Collaboration XVII 2011; Gordon et al. 2014). Several explanations have been proposed including a very cold dust component (<10 K), spinning dust (Anderson & Watson 1993; Draine & Lazarian 1998a,b), the Two-Level-System of amorphous dust (Meny et al. 2007), or a broken dust emissivity law model (where the emissivity changes at a 'break wavelength' Li & Draine 2001). Explanations invoking very cold dust are problematic as they lead to very large estimated dust masses. In the LMC Gordon et al. (2014) found the broken emissivity law model had the lowest residuals. These models will be investigated in detail in Paper V (Lamperti et al., in preparation).

The FIR colours that we have been studying can be used as an indicator of the cold dust temperature $T_{\rm dust}$ and emissivity index β (e.g. Galametz et al. 2010; Boselli et al. 2010b; Bendo et al. 2012; Boselli et al. 2012; Dale et al. 2012; Rémy-Ruyer et al. 2013; Cortese et al. 2014). We investigate which IR continuum flux ratios have the strongest correlation with $T_{\rm dust}$ and β, measured from a modified blackbody fit including the 850 μm fluxes (see Fig. 13). This can be useful for surveys that do not have the wavelength coverage to do full SED fitting.

Fig. 13, shows the same FIR/sub-mm colour ratios versus our calculated dust emissivity index and dust temperature. In each panel we compute the Pearson correlation coefficient (ρ), for all objects with a signal-to-noise ratio greater than 3. The flux ratios F_{100}/F_{160} and F_{100}/F_{250} have the strongest correlations with the dust temperature ($\rho = 0.68$ and 0.58, respectively). These flux bands are sampling the peak of the SED, which for a typical dust temperature between 10 and 30 K is in the wavelength range 90–250 μm. There are also fairly strong negative correlations with $\rho = -0.53$ and -0.54, between dust temperature and the F_{160}/F_{850} or F_{250}/F_{850}, respectively. We do not investigate these further, but these may arise due to a temperature-β degeneracy (for more discussion see Paper V, Lamperti et al., in preparation).

The flux ratio F_{160}/F_{850} has the strongest correlation with the emissivity index β ($\rho = 0.82$), closely followed by the F_{250}/F_{850} with $\rho = 0.76$. These colour-ratios are sampling the Rayleigh–Jeans tail of the sub-millimeter SED, and therefore are a good proxy of β. We fit the distribution of FIR/submm colour (with signal-noise ratios greater than 3) to either dust temperature or β, assuming this model:

$$F_i/F_j = \gamma 10^{\alpha X} \tag{8}$$

where F_i and F_j are the fluxes in the FIR/submm bands, α and γ are the model parameters, and X is either dust temperature or β. We fit this model rather than a straight line to $\log_{10}(F_i/F_j)$ as the flux uncertainties are assumed Gaussian in the linear regime. We perform the fits using the PYMC3 package (Salvatier, Wiecki & Fonnesbeck 2016), and incorporate uncertainties in both FIR/submm colour and dust model parameters. Table 3 shows the correlation coefficients, and the fitted model parameters to relate the FIR/submm colours with β or dust temperature. These fits can be used to estimate $T_{\rm dust}$ and β if only two flux points are available.

For comparison, in Table 3 we also include the correlation coefficients and fits possible with only *Herschel* data. For estimates of β we note the correlation is better if longer wavelength information is available (e.g. $\rho = 0.54$ for F_{250}/F_{500} versus $\rho = 0.79$ for F_{250}/F_{850}).

6.4 Far-infrared colours versus galaxy physical parameters

In this final section we investigate if there are any relationships between the FIR/sub-mm colours and a few physical parameters of the galaxy from the quantities calculated in Paper I. We look for correlations with SFR, stellar mass (M_*), specific star-formation rate (SFR/M_*), the surface density of SFR (Σ(SFR)), and the surface density of stellar mass (Σ_*). The two surface densities are calculated based on taking the integrated quantity (i.e. SFR or M_*) and dividing by the elliptical area of the galaxy using the Petrosian radius (in kpc) and the axial ratio of each galaxy.

Fig. 14 shows the FIR colours versus the various physical properties defined above. The best correlation with a Spearman rank coefficient of $\rho = 0.57$ is between $\Sigma(SFR)$ and the F_{160}/F_{500} (closely followed by the F_{100}/F_{250} and F_{250}/F_{500}), and similar, but reduced correlations are also seen with the SFR. Correlations with Σ(SFR) and SFR would be expected due to the strength of the interstellar radiation field leading to an increase of the dust temperature, or equivalently FIR luminosity is used as a star formation tracer (e.g. Kennicutt 1998). Surprisingly, from Section 6.3 both the F_{160}/F_{500} and F_{250}/F_{500} colours are better tracers of β, rather than dust temperature. This will be further investigated in Lamperti et al. (in preparation). There are also some weak correlations with stellar mass and stellar mass surface density which again may be the effect of increasing the interstellar radiation field and therefore increasing the dust temperature; however, our results suggest for the majority of galaxies in JINGLE this is less significant than the heating from star formation.

Boselli et al. (2012) also compared their FIR colour-ratios for the HRS sample to a similar set of physical galaxy properties. For both samples a correlation is found between FIR colours at longer wavelength and the Σ_* (or equivalently in the HRS study

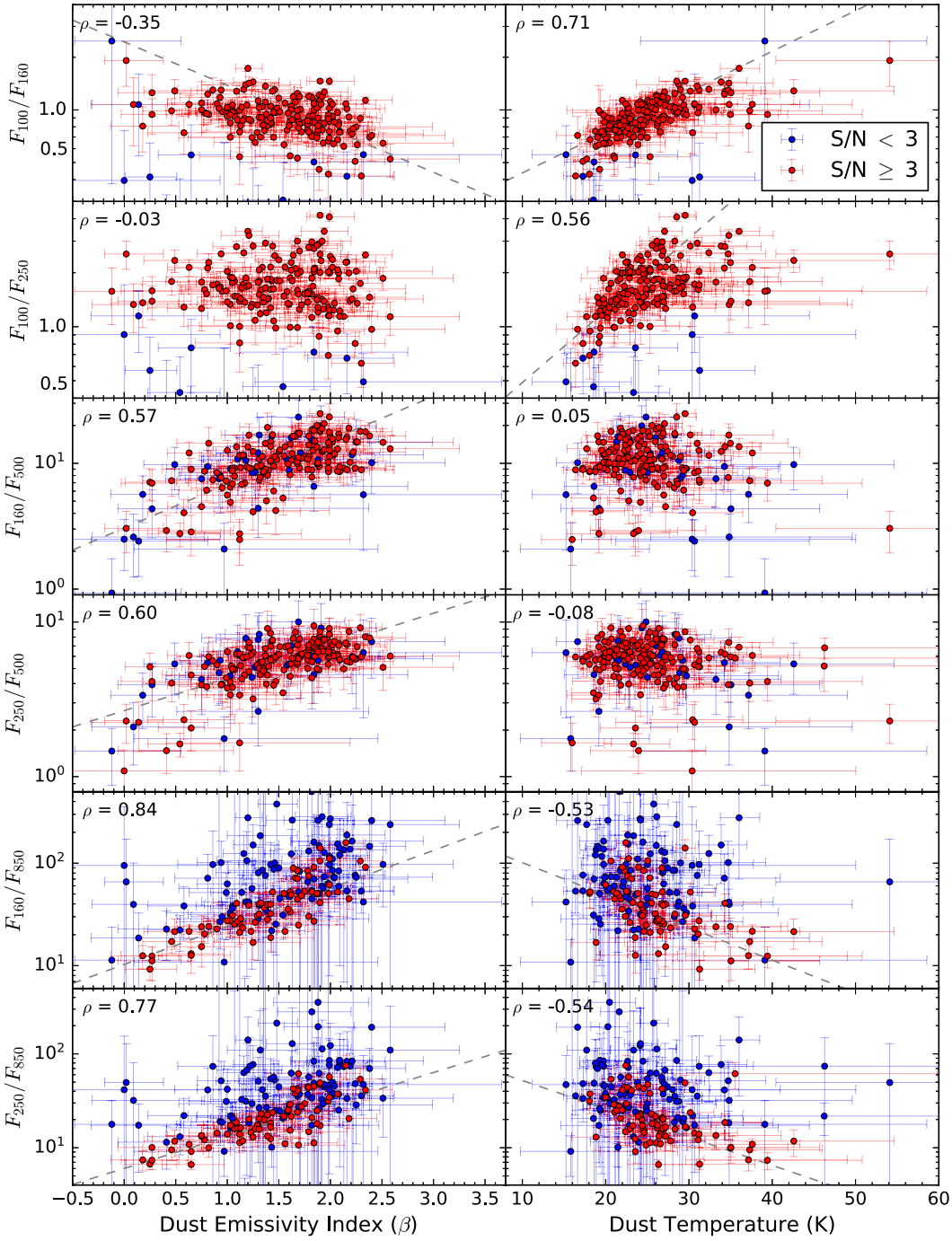

Figure 13. Correlation between flux ratios and the dust emissivity β (left) and dust temperature (right). In blue are shown points for which one of the flux measurements has high uncertainties (S/N $<$ 3). The Pearson correlation coefficients ρ for the objects with a signal-to-noise greater than 3 is shown in the top-left of each panel. The flux ratios F_{100}/F_{160} and F_{100}/F_{250} have the strongest correlation with the dust temperature ($\rho = 0.68$ and $\rho = 0.58$, respectively), although there are also negative correlations with the F_{160}/F_{850} and F_{250}/F_{850}. The flux ratio F_{160}/F_{850} and F_{250}/F_{850} show the best correlation with β (with $\rho = 0.82$ and 0.76, respectively). The grey lines show the best-fitting models specified in Table 3. Due to the large scatter of the lower signal-to-noise data points, a few objects may lie outside the plotted range.

H-band surface brightness). Surprisingly, Boselli et al. (2012) did not find any correlations with SFR (although correlations with Hα surface density were found), this may be due to the different methods of measuring SFR (dust extinction-corrected Hα or FUV emission versus panchromatic SED fitting for JINGLE), or the greater fraction of early-type galaxies in the HRS.

7 CONCLUSIONS

In this paper, we have presented new SCUBA-2 data of the JINGLE sample which consists of 193 galaxies in the range 41–212 Mpc. We described our data reduction tests and techniques which attempt to optimize the SCUBA-2 data for the case of slightly extended galaxies, going beyond what is performed in the standard SCUBA-

Table 3. Correlation between flux ratios and dust properties (temperature and β).

Flux ratio	Dust emissivity index (β)			Dust temperature		
	ρ	α	γ	ρ	α (K^{-1})	γ
F_{100}/F_{160}	−0.35	−0.248 ± 0.016	2.45 ± 0.15	0.71	0.0232 ± 0.0013	0.256 ± 0.019
F_{100}/F_{250}	−0.03	–	–	0.56	0.0402 ± 0.0190	0.194 ± 0.020
F_{160}/F_{500}	0.57	0.349 ± 0.019	3.06 ± 0.22	0.05	–	–
F_{250}/F_{500}	0.60	0.210 ± 0.013	2.67 ± 0.14	−0.08	–	–
F_{160}/F_{850}	0.84	0.371 ± 0.031	10.3 ± 1.01	−0.53	−0.0317 ± 0.0036	210.0 ± 52.6
F_{250}/F_{850}	0.77	0.305 ± 0.030	6.02 ± 0.56	−0.54	−0.0301 ± 0.0035	104.0 ± 25.4

Notes. The table provides the Spearman rank coefficient (ρ), and model parameters for our distributions of FIR/submm colours versus fitted dust parameters. For the model parameters described in equation (8) the median of the posterior distribution is given, and its uncertainty estimated from the 16th and 84th percentile (the uncertainties are to a good approximation symmetrical). We only provide model fits for the parameters for distributions with $|\rho| > 0.3$.

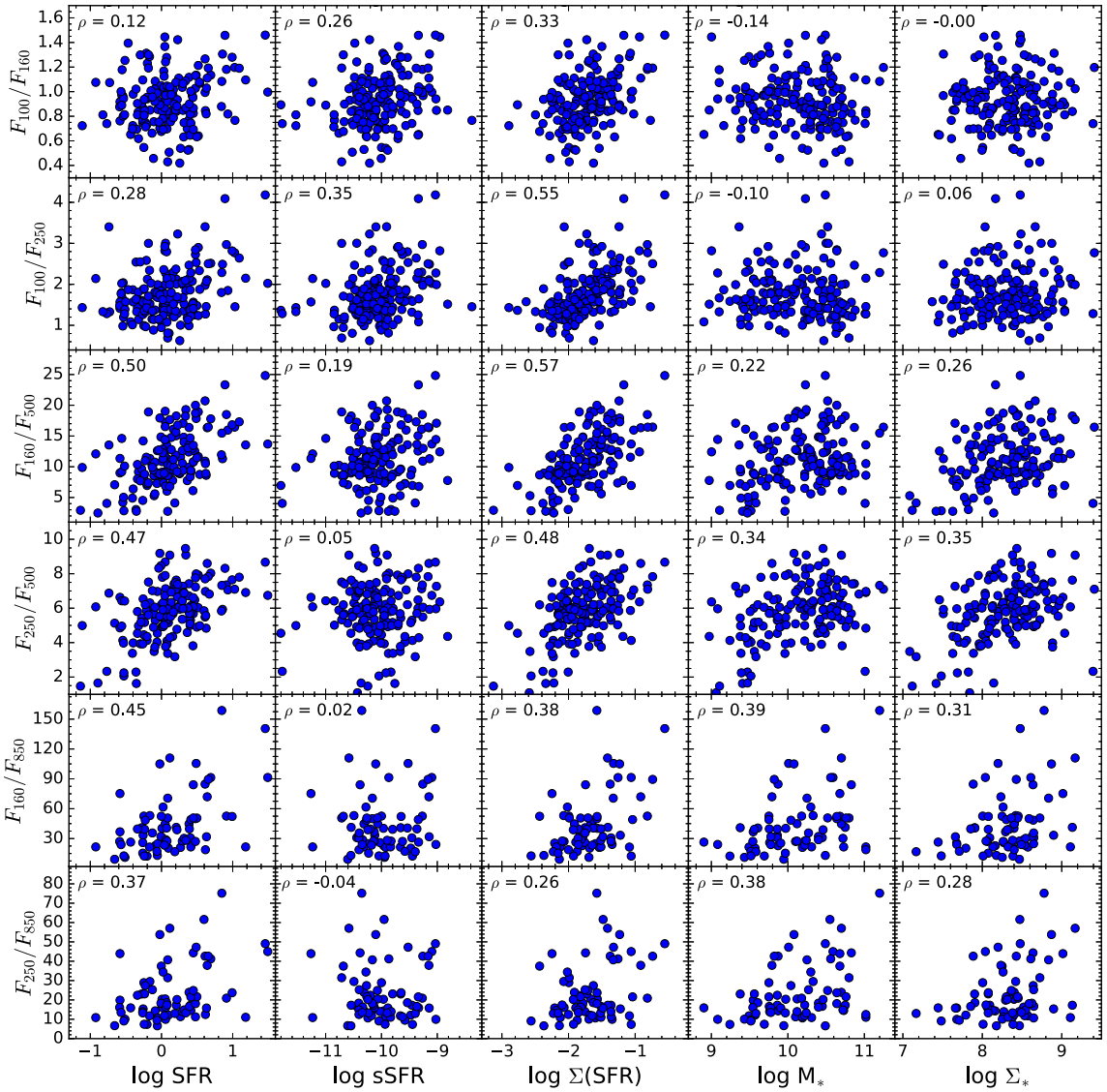

Figure 14. FIR colours versus the SFR, sSFR, Σ(SFR), M_*, and Σ_*, as defined in Section 6.4. The Spearman rank correlation for each panel is shown in the top left hand corner. Data points are included if the flux densities used to create each FIR/sub-mm colour have a signal-to-noise of at least 3.

2 pipeline. We investigate the optimum parameters, calibration, and offset corrections for our data. By incorporating data from *Herschel* (both PACS and SPIRE) and WISE, we measure aperture-matched global fluxes across the dust SED. Our measurements attempt to account for aperture corrections, effects from the pipeline filtering in the SCUBA-2 wavelengths, all sources of noise in the FIR wavelengths (e.g. instrumental, confusion, cirrus, etc.), and the contamination from the CO($J = 3 - 2$) line.

Using the *Herschel* data we find that the FIR/submm colours are similar to the HRS, and we find similar results to Boselli et al. (2012), that the distribution on colour–colour plots appears incompatible with an SMBB with a constant β, but the majority of galaxies could be described with β in the standard range of 1.5–2.0. By adding our 850 μm fluxes, we find that approximately half of the JINGLE objects require a value of β significantly lower than 1.5. Such low values are hard to reproduce with lower temperatures and so possibly indicate a more complicated dust model like those that have a broken-emissivity law is required. The distribution of JINGLE galaxies confirms one dust model cannot explain the entire sample. These models applied to individual objects will be further investigated by Lamperti et al. (in preparation) who will use a Bayesian hierarchical fitting approach.

We found that the F_{160}/F_{850} and the F_{250}/F_{850} colours have the strongest correlation ($\rho = 0.84$ and 0.77, respectively) with β estimated from an SMBB model. The dust temperature is better correlated with shorter wavelength colours from *Herschel* data, with the highest correlation found for the F_{100}/F_{160} colour ($\rho = 0.71$). We provide the fits to these plots to find an estimate of β and temperature from a FIR/submm colour.

Finally, we investigate how the FIR/submm colours vary with different physical parameters presented in Paper I. The best correlation is between the FIR/submm colour and the surface density of SFR (closely followed by the total SFR), indicating that for JINGLE galaxies dust heating is predominantly due to young-stellar populations rather than older stellar populations. However, there is a significant but reduced correlation with stellar surface density, suggesting some dust heating from older stellar populations occurs in JINGLE galaxies.

ACKNOWLEDGEMENTS

MWLS acknowledges support from the European Research Council (ERC) Forward Progress 7 (FP7) project HELP. MWLS acknowledges funding from the UK Science and Technology Facilities Council consolidated grant ST/K000926/1.

EB acknowledges support from STFC, grant number ST/M001008/1.

IDL gratefully acknowledges the support of the Research Foundation Flanders (FWO).

HG acknowledges support from the European Research Council (ERC) in the form of Consolidator grant COSMICDUST.

The James Clerk Maxwell Telescope is operated by the East Asian Observatory on behalf of The National Astronomical Observatory of Japan; Academia Sinica Institute of Astronomy and Astrophysics; the Korea Astronomy and Space Science Institute; the Operation, Maintenance and Upgrading Fund for Astronomical Telescopes and Facility Instruments, budgeted from the Ministry of Finance (MOF) of China and administrated by the Chinese Academy of Sciences (CAS), as well as the National Key R&D Program of China (No. 2017YFA0402700). Additional funding support is provided by the Science and Technology Facilities Council of the United Kingdom and participating universities in the United Kingdom and Canada.

We thank everyone involved with the *Herschel Space Observatory*.

SPIRE has been developed by a consortium of institutes led by Cardiff University (UK) and including: University of Lethbridge (Canada); NAOC (China); CEA, LAM (France); IFSI, University of Padua (Italy); IAC (Spain); Stockholm Observatory (Sweden); Imperial College London, RAL, UCL-MSSL, UKATC, University of Sussex (UK); and Caltech, JPL, NHSC, University of Colorado (USA). This development has been supported by national funding agencies: CSA (Canada); NAOC (China); CEA, CNES, CNRS (France); ASI (Italy); MCINN (Spain); SNSB (Sweden); STFC, UKSA (UK); and NASA (USA).

This research made use of Astropy, a community-developed core Python package for Astronomy (Astropy Collaboration 2013).

REFERENCES

Anderson N., Watson W. D., 1993, A&A, 270, 477
Astropy Collaboration, 2013, A&A, 558, A33
Bauermeister A., Blitz L., Bolatto A., Bureau M., Teuben P., Wong T., Wright M., 2013, ApJ, 763, 64
Bendo G. J. et al., 2006, ApJ, 652, 283
Bendo G. J. et al., 2012, MNRAS, 419, 1833
Bendo G. J. et al., 2013, MNRAS, 433, 3062
Bianchi S., 2013, A&A, 552, A89
Boselli A. et al., 2010a, PASP, 122, 261
Boselli A. et al., 2010b, A&A, 518, L61
Boselli A. et al., 2012, A&A, 540, A54
Boselli A., Cortese L., Boquien M., 2014a, A&A, 564, A65
Boselli A., Cortese L., Boquien M., Boissier S., Catinella B., Lagos C., Saintonge A., 2014b, A&A, 564, A66
Bot C., Ysard N., Paradis D., Bernard J. P., Lagache G., Israel F. P., Wall W. F., 2010, A&A, 523, A20
Bothwell M. S., Maiolino R., Kennicutt R., Cresci G., Mannucci F., Marconi A., Cicone C., 2013, MNRAS, 433, 1425
Bryant J. J. et al., 2015, MNRAS, 447, 2857
Bundy K. et al., 2015, ApJ, 798, 7
Calzetti D., 2001, PASP, 113, 1449
Catinella B. et al., 2010, MNRAS, 403, 683
Chapin E. L., Berry D. S., Gibb A. G., Jenness T., Scott D., Tilanus R. P. J., Economou F., Holland W. S., 2013, MNRAS, 430, 2545
Ciesla L. et al., 2012, A&A, 543, A161
Clark C. J. R. et al., 2015, MNRAS, 452, 397
Clark C. J. R., Schofield S. P., Gomez H. L., Davies J. I., 2016, MNRAS, 459, 1646
Clemens M. S. et al., 2013, MNRAS, 433, 695
Cortese L. et al., 2012, A&A, 540, A52
Cortese L. et al., 2014, MNRAS, 440, 942
Cortese L., Catinella B., Boissier S., Boselli A., Heinis S., 2011, MNRAS, 415, 1797
Corwin H. G. Jr, Buta R. J., de Vaucouleurs G., 1994, AJ, 108, 2128
Currie M. J., Berry D. S., Jenness T., Gibb A. G., Bell G. S., Draper P. W., 2014, in Manset N., Forshay P., eds, ASP Conf. Ser. Vol. 485, Astronomical Data Analysis Software and Systems XXIII. Astron. Soc. Pac., San Francisco, p. 391
Dale D. A. et al., 2012, ApJ, 745, 95
De Vis P. et al., 2017, MNRAS, 464, 4680
Dempsey J. T. et al., 2013, MNRAS, 430, 2534
Drabek E. et al., 2012, MNRAS, 426, 23
Draine B. T., Lazarian A., 1998a, ApJ, 494, L19
Draine B. T., Lazarian A., 1998b, ApJ, 508, 157
Dumke M., Krause M., Wielebinski R., 2004, A&A, 414, 475
Eales S. et al., 2010, PASP, 122, 499
Foreman-Mackey D., Hogg D. W., Lang D., Goodman J., 2013, PASP, 125, 306
Galametz M. et al., 2009, A&A, 508, 645
Galametz M. et al., 2010, A&A, 518, L55
Galametz M. et al., 2012, MNRAS, 425, 763
Galliano F., Madden S. C., Jones A. P., Wilson C. D., Bernard J.-P., Le Peintre F., 2003, A&A, 407, 159
Geach J. E. et al., 2017, MNRAS, 465, 1789
Giovanelli R. et al., 2005, AJ, 130, 2598
Goodman J., Weare J., 2010, Commun. Appl. Math. Comput. Sci., 5, 65
Gordon K. D. et al., 2014, ApJ, 797, 85

Gould R. J., Salpeter E. E., 1963, ApJ, 138, 393
Guelin M., Zylka R., Mezger P. G., Haslam C. G. T., Kreysa E., Lemke R., Sievers A. W., 1993, A&A, 279, L37
Guelin M., Zylka R., Mezger P. G., Haslam C. G. T., Kreysa E., 1995, A&A, 298, L29
Hagen W., Allamandola L. J., Greenberg J. M., 1979, Ap&SS, 65, 215
Hildebrand R. H., 1983, QJRAS, 24, 267
Hunt L. K. et al., 2015, A&A, 576, A33
Israel F. P., 1997, A&A, 328, 471
Israel F. P., Wall W. F., Raban D., Reach W. T., Bot C., Oonk J. B. R., Ysard N., Bernard J. P., 2010, A&A, 519, A67
Ivison R. J. et al., 2016, ApJ, 832, 78
Jones E. et al., 2001, SciPy: Open source scientific tools for Python
Kennicutt R. C. et al., 2011, PASP, 123, 1347
Kennicutt R. C. Jr, 1989, ApJ, 344, 685
Kennicutt Robert C. J. et al., 2003, PASP, 115, 928
Kennicutt Robert C. J., 1998, ARA&A, 36, 189
Kirkpatrick A. et al., 2014, ApJ, 789, 130
Lagache G., Puget J.-L., Dole H., 2005, ARA&A, 43, 727
Leroy A. K. et al., 2009, AJ, 137, 4670
Li A., Draine B. T., 2001, ApJ, 554, 778
Lis D. C., Serabyn E., Keene J., Dowell C. D., Benford D. J., Phillips T. G., Hunter T. R., Wang N., 1998, ApJ, 509, 299
Lisenfeld U. et al., 2011, A&A, 534, A102
Lisenfeld U., Israel F. P., Stil J. M., Sievers A., 2002, A&A, 382, 860
Maddox S. J. et al., 2018, ApJS, 236, 30
Mairs S. et al., 2015, MNRAS, 454, 2557
Mao R.-Q., Schulz A., Henkel C., Mauersberger R., Muders D., Dinh-V-Trung, 2010, ApJ, 724, 1336
Mauersberger R., Henkel C., Walsh W., Schulz A., 1999, A&A, 341, 256
Meny C., Gromov V., Boudet N., Bernard J. P., Paradis D., Nayral C., 2007, A&A, 468, 171
Nguyen H. T. et al., 2010, A&A, 518, L5
Papadopoulos P. P., van der Werf P., Xilouris E., Isaak K. G., Gao Y., 2012, ApJ, 751, 10
Parsons H. et al., 2018, ApJS, 234, 22
Pilbratt G. L. et al., 2010, A&A, 518, L1
Planck Collaboration XVII, 2011, A&A, 536, A17
Planck Collaboration XIV, 2014, A&A, 564, A45
Pohlen M. et al., 2010, A&A, 518, L72
Rela no M. et al., 2018, A&A, 613, A43
Rémy-Ruyer A. et al., 2013, A&A, 557, A95
Rémy-Ruyer A. et al., 2014, A&A, 563, A31
Roberts M. S., Haynes M. P., 1994, ARA&A, 32, 115
Saintonge A. et al., 2011, MNRAS, 415, 32
Saintonge A. et al., 2018, MNRAS, 481, 3497 (Paper I)
Salvatier J., Wiecki T. V., Fonnesbeck C., 2016, Astrophysics Source Code Library, record ascl:1610.016
Schmidt M., 1959, ApJ, 129, 243
Scoville N. et al., 2014, ApJ, 783, 84
Smith M. W. L. et al., 2012a, ApJ, 748, 123
Smith M. W. L. et al., 2012b, ApJ, 756, 40
Smith M. W. L. et al., 2016, MNRAS, 462, 331
Smith M. W. L. et al., 2017, ApJS, 233, 26
Smith M., 2013, PhD thesis. Univ. Cardiff
Solomon P. M., Downes D., Radford S. J. E., Barrett J. W., 1997, ApJ, 478, 144
Tabatabaei F. S. et al., 2014, A&A, 561, A95
Valiante E. et al., 2016, MNRAS, 462, 3146
van Dishoeck E. F., 2004, ARA&A, 42, 119
Walter F., Brinks E., de Blok W. J. G., Bigiel F., Kennicutt Robert C. J., Thornley M. D., Leroy A., 2008, AJ, 136, 2563
Ward-Thompson D. et al., 2007, PASP, 119, 855
Yao L., Seaquist E. R., Kuno N., Dunne L., 2003, ApJ, 588, 771
Young J. S. et al., 1995, ApJS, 98, 219
Young L. M. et al., 2011, MNRAS, 414, 940

SUPPORTING INFORMATION

Supplementary data are available at *MNRAS* online.

JINGLE-DR1-FluxTable.fits

Please note: Oxford University Press is not responsible for the content or functionality of any supporting materials supplied by the authors. Any queries (other than missing material) should be directed to the corresponding author for the article.

[1]*School of Physics and Astronomy, Cardiff University, Queens Buildings, The Parade, Cardiff CF24 3AA, UK*
[2]*Space Telescope Science Institute, 3700 San Martin Drive, Baltimore, MD 21218, USA*
[3]*Department of Physics & Astronomy, University College London, Gower Street, London WC1E 6BT, UK*
[4]*Sterrenkundig Observatorium, Ghent University, Krijgslaan 281 - S9, B-9000 Gent, Belgium*
[5]*Department of Physics & Astronomy, McMaster University, Hamilton, ON L8S 4M1 Canada*
[6]*Centre for Astrophysics Research, University of Hertfordshire, College Lane AL10 9AB, UK*
[7]*Sub-department of Astrophysics, University of Oxford, Denys Wilkinson Building, Keble Road, Oxford OX1 3RH, UK*
[8]*Yonsei Frontier Lab and Department of Astronomy, Yonsei University, 50 Yonsei-ro, Seodaemun-gu, Seoul 03722, Republic of Korea*
[9]*Korea Astronomy and Space Science Institute, 776 Daedeokdae-ro, Yuseong-gu, Daejeon 34055, South Korea*
[10]*Blackett Laboratory, Physics Department, Imperial College, London SW7 2AZ, UK*
[11]*Academia Sinica, Institute of Astronomy and Astrophysics, No. 1, Section 4, Roosevelt Road, 10617 Taipei, Taiwan*
[12]*National Central University, No. 300, Zhongda Road, Zhongli District, Taoyuan City 32001, Taiwan*
[13]*Shanghai Astronomical Observatory, 80 Nandan Road, Xuhui District, Shanghai 200030, China*
[14]*Purple Mountain Observatory, Chinese Academy of Sciences, Nanjing 210034, China*
[15]*School of Physics, Korea Institute for Advanced Study, 85 Hoegiro, Dongdaemun-gu, Seoul 02455, South Korea*
[16]*European Southern Observatory, Karl-Schwarzchild-Str. 2, D-85748 Garching b. München, Germany*
[17]*Department of Astronomy, Tsinghua University, Beijing 100084, China*
[18]*Astronomy Centre, Department of Physics and Astronomy, University of Sussex, Brighton BN1 9QH, England*
[19]*INAF - Osservatorio Astronomico di Cagliari, Via della Scienza 5, I-09047 Selargius (CA), Italy*
[20]*Department of Physics & Astronomy, University of Toledo, Toledo, OH 43606, USA*
[21]*School of Physical Sciences, The Open University, Walton Hall, Milton Keynes MK7 6AA, UK*
[22]*Key Laboratory of Radio Astronomy, Chinese Academy of Sciences, Nanjing 210008, China*
[23]*European Southern Observatory, Alonso de Córdova 3107, Casilla 19001, Victacura, Santiago, Chile*
[24]*National Astronomical Observatory of China, 20A Datun Road, Chaoyang District, Beijing 100012, China*

This paper has been typeset from a TEX/LATEX file prepared by the author.